MECHANICAL METRICS OF THE PROXIMAL FEMUR ARE PRECISE AND ASSOCIATED WITH HIP MUSCLE PROPERTIES: A MAGNETIC RESONANCE BASED FINITE ELEMENT STUDY

A Thesis Submitted to the

College of Graduate and Postdoctoral Studies

In Partial Fulfillment of the Requirements

For the Degree of Master of Science

In the Department of Mechanical Engineering

University of Saskatchewan

Saskatoon

By

KADIN BRANDT MAJCHER

PERMISSION TO USE

In presenting this thesis/dissertation in partial fulfillment of the requirements for a Postgraduate degree from the University of Saskatchewan, I agree that the Libraries of this University may make it freely available for inspection. I further agree that permission for copying of this thesis/dissertation in any manner, in whole or in part, for scholarly purposes, may be granted by the professor or professors who supervised my thesis/dissertation work or, in their absence, by the Head of the Department or the Dean of the College in which my thesis work was done. It is understood that any copying or publication or use of this thesis/dissertation or parts thereof for financial gain shall not be allowed without my written permission. It is also understood that due recognition shall be given to me and to the University of Saskatchewan in any scholarly use which may be made of any material in my thesis/dissertation.

DISCLAIMER

Reference in this thesis/dissertation to any specific commercial products, process, or service by trade name, trademark, manufacturer, or otherwise, does not constitute or imply its endorsement, recommendation, or favoring by the University of Saskatchewan. The views and opinions of the author expressed herein do not state or reflect those of the University of Saskatchewan, and shall not be used for advertising or product endorsement purposes.

Requests for permission to copy or to make other uses of materials in this thesis/dissertation in whole or part should be addressed to:

Head of the Department of Mechanical Engineering
57 Campus Drive
University of Saskatchewan
Saskatoon, Saskatchewan S7N 5A9 Canada

OR

Dean
College of Graduate and Postdoctoral Studies
University of Saskatchewan
116 Thorvaldson Building, 110 Science Place
Saskatoon, Saskatchewan S7N 5C9 Canada

ABSTRACT

Proximal femoral (hip) fractures are a life-threatening injury which affects 30,000 Canadians annually. Improved muscle and bone strength assessment methods may reduce fracture occurrence rates in the future. Magnetic resonance (MR) imaging has potential to assess proximal femoral bone strength *in vivo* through usage of finite element (FE) modeling. Though, to precisely assess bone strength, knowledge of a technique's measurement error is needed. Hip muscle properties (e.g., lean muscle and fat area) are intrinsically linked to proximal femoral bone strength; however, it is unclear which muscles and properties are most closely associated with bone strength.

This thesis is focused on MR-based FE modeling (MR-FE) of the proximal femur and surrounding muscle properties (e.g., hip abductor fat area, hip extensor muscle area). The specific objectives of this research were 1) to characterize the short-term *in vivo* measurement precision of MR-FE outcomes (e.g., failure load) of the proximal femur for configurations simulating fall and stance loading, and 2) explore associations between upper thigh muscle and fat properties (e.g., hip abductor fat area, knee extensor muscle area) with MR-FE failure loads of the proximal femur.

In vivo precision errors (assessed via root mean square coefficient of variation, $CV\%_{RMS}$ from repeated measures) of MR-FE outcomes ranged from 3.3-11.8% for stress and strain outcomes, and 6.0-9.5% for failure loads. Hip adductor muscle area and total muscle area correlated with failure load of the fracture-prone neck and intertrochanteric region under both fall and stance loading (correlation coefficients ranged from 0.416-0.671).

This is the first study to report the *in vivo* short-term precision errors of MR-FE outcomes at the proximal femur. Also, this is the first study to relate upper-thigh muscle and fat properties with MR-FE derived failure loads. Results indicate that MR-FE outcomes have comparable precision to computed tomography (CT) based FE outcomes and are related to hip muscle area.

PREFACE

Chapters 4 and 5 of this thesis have been drafted as co-authored manuscripts. I have provided contributions of the co-authors for both manuscripts-in-progress below.

Manuscript 1 – Chapter 4:

Majcher KB, Kontulainen SA, Leswick DA, Dolovich AT, Johnston JD. MR-FE Modeling of the Proximal Femur: an *in vivo* precision study. *Manuscript in preparation.*

Authors' contributions: Kadin Majcher was jointly responsible for performing the image analyses, finite element analysis, data analysis, statistical analyses, data interpretation, and drafted the manuscript. Dr. Saija Kontulainen assisted with statistical analyses and was jointly responsible for the original ideas and was a key editor. Dr. David Leswick was involved in the original study design and assisted in the image analysis. Dr. JD Johnston was jointly responsible for the original ideas, image and data analysis, and was a key editor.

The results of this study were presented at national and international conferences:

i. Majcher KB, Kontulainen SA, Leswick DA, Johnston JD. Magnetic resonance imaging based finite element modeling of the proximal femur: an *in vivo* precision study. The International Society of Biomechanics Symposium, Calgary, AB, August 2019.

ii. Majcher KB, Kontulainen SA, Leswick DA, Johnston JD. *In vivo* precision of magnetic resonance imaging based finite element outcomes of the proximal femur. Life and Health Sciences Research Expo, University of Saskatchewan, Saskatoon, SK, May 2019.

Manuscript 2 – Chapter 5:

Majcher KB, Kontulainen SA, Leswick DA, Johnston JD. Association of Hip Muscle and Fat Properties with MR-FE Derived Failure Load of the Proximal Femur. *Manuscript in preparation.*

Authors' contributions: Kadin Majcher was jointly responsible for performing the image analyses, finite element analysis, data analysis, statistical analyses, data interpretation, and drafted the manuscript. Dr. Saija Kontulainen assisted with statistical analyses and was jointly responsible for the original ideas and was a key editor. Dr. David Leswick was involved in the original study design. Dr. JD Johnston was jointly responsible for the original ideas, image and data analysis, and was a key editor.

ACKNOWLEDGMENTS

Thank you to my supervisors, Dr. JD Johnston and Dr. Saija Kontulainen for their guidance, encouragement, and support throughout my studies. Without their continual help, this project would not have been possible. I have greatly enjoyed working alongside each of you.

Thank you to my friends and colleagues for their on-going support, suggestions, and Winter Wednesday's. I am grateful for the continual encouragement I would not have been able to complete this project without you.

I would like to thank my family for supporting me on this academic journey. Your words of encouragement and evening phone calls helped make this thesis a success.

TABLE OF CONTENTS

LIST OF TABLES

LIST OF FIGURES

LIST OF ABBREVIATIONS

Abbreviation	Description
2D	Two dimensional
3D	Three dimensional
aBMD	Areal bone mineral density (g/cm^2)
BCM	Brittle Coulomb-Mohr
BMI	Body Mass Index (kg/m^2)
BVF	Bone volume fraction
BW	Body weight
CT	Computed tomography
CV%	Percentage of coefficient of variation
DOF	Degrees-of -freedom
DXA	Dual energy X-ray absorptiometry
FE	Finite element
HMH	Half maximum height
HSA	Hip Strength Analysis
HU	Hounsfield units
InterMAT	Intermuscular adipose tissue
IntraMAT	Intramuscular adipose tissue
MRI	Magnetic resonance imaging
MR	Magnetic resonance
MR-FE	Magnetic resonance imaging based finite element modeling
PBMAS	Saskatchewan Pediatric Bone Mineral Accrual Study

RF	Radio frequency
ROI	Region of interest
RMS	Root mean square
SD	Standard deviation
TE	Echo time (ms)
TR	Relaxation time (ms)
TV	Total volume
vBMD	Volumetric bone mineral density (g/cm^3)

GLOSSARY

Term	Definition
Anterior	Frontal plane of the body, facing forward
Acetabulofemoral joint	The joint between the femur and acetabulum of the pelvis. Commonly referred to as the hip joint
Apparent Density	Wet weight divided by the bone tissue volume (g/cm^3)
Ash Density	Ash weight divided by the bone tissue volume (g/cm^3)
Areal bone mineral density	DXA measure of bone mineral density per image area (g/cm^2)
Body mass index	Body mass divided by the square of the body height (kg/m^2)
Bone mineral density	Bone mass within a specific volume
Bone volume fraction	The volume of mineralized bone per unit volume (BV/TV)
Coronal	Plane that divides the body into anterior and posterior sections
Cortical bone	The compact bone tissue, or outer shell of bone; more dense than trabecular bone
Distal	Pertaining to the end of an extremity situated furthest from the center of the body
In vivo	Latin for "within the living;" an experiment taking place inside of a living organism
Intramuscular adipose tissue	The fat infiltrated between and/or within muscle fibers (IntraMAT)
Intermuscular adipose tissue	The fat between adjacent muscle groups (IMAT)
Poisson's ratio	Ratio of transverse to longitudinal strains
Posterior	Rear plane of the body, facing back

Proximal	Pertaining to the end of an extremity situated nearest to the center of the body (the proximal femur is located near the acetabulofemoral joint)
Sagittal	Plane that travels from the top to the bottom of a body, dividing it into left and right portions
Trabecular bone	The cancellous bone tissue, cellular-like; less dense than cortical bone
Transverse	Plane that divides the body into superior and inferior sections
Voxel	Volume element in three-dimensional space

CHAPTER 1
OVERVIEW

1.1 Introduction

Annually in Canada, approximately 30,000 people experience a hip fracture [1], most commonly at the proximal femur. These fractures typically result in life-altering outcomes which include chronic pain, depression, and mortality [2]. Hip fracture risk increases with age, with over 90% of fracture patients aged 65 years or older [3]. Morphologically, people with osteoporosis are predisposed to an increased risk of fracture due to low bone strength and microstructural deterioration [4]. Proximal femoral fractures primarily occur by a sideways fall from standing height, with elderly women (≥75 years of age) being at an increased risk [5]. Fracture occurs when the applied external forces on the bone exceed the bone strength, or failure load.

A preemptive, non-invasive assessment of proximal femoral strength can provide early indication of fracture risk and may assist in prescribing preventative measures. Dual-energy X-ray absorptiometry (DXA) is the current gold-standard technique for estimating proximal femoral strength and propensity for fracture. DXA provides non-invasive two-dimensional (2D) measures of areal bone mineral density (aBMD), with an individual classified as osteoporotic/osteopenia if their aBMD lies at least 2.5 standard deviations below the average aBMD for a young healthy adult person (T-score <2.5) [6]. Low aBMD measures are associated with an increased risk of fracture at population levels [7]; though, aBMD is a poor predictor of fracture risk at individual levels, in part due to the limitation of aBMD to estimate bone strength [8]. To this point, approximately half of all hip fractures occur in individuals that are not considered at risk according to aBMD measures [9]. Improved methods are needed for characterizing proximal femoral strength to assist in prevention and treatment of hip bone fragility.

Advanced three-dimensional (3D) *in vivo* imaging modalities can be used to provide information pertaining to bone strength beyond DXA [10]. Magnetic resonance (MR) imaging (also known as MRI) is a multi-planar technology that can be safely used in combination with finite element (FE) modeling for non-invasive assessment of proximal femoral mechanical outcomes (e.g., stress, strain, failure load). MR-based FE (referred to as MR-FE) analysis can directly model bone geometry from the image, with bone material properties (e.g., elastic modulus, strength) derived from image intensity [11]. MR-FE is a relatively new, less-explored method, with a few studies showing its potential to be used in characterizing bone strength. At present, *in vivo* precision errors of previously used FE outcomes obtained from MR-FE are currently unknown. This is important as precision error information is needed to assess the validity of strength estimates.

Precision aside, the proximal femoral bone strength is intrinsically linked to the surrounding muscles as the greatest forces habitually applied to bone arise from muscular contractions. According to the mechanostat theory, the skeleton is a biomechanically-regulated structure, with strength adaptation modulated by the applied loading (via muscle forces or dynamic loading) [12,13]. Skeletal bones respond and adapt to loading stimulation, with the material distribution acting as a feedback system to optimize strength [12,14]. As prior studies have shown that muscle plays a role in bone adaptation and geometry, it is important to include upper-thigh muscle and fat measures when evaluating hip strength [15,16]. It is currently unknown how muscle properties (e.g., muscle area, fat area) at the hip are related to bone structural properties (e.g., failure load). Improved understanding of how muscle forces are associated with structural properties of bone may guide investigations in the development of preventative strategies aiming to reduce the risk of fracture (e.g., muscle exercise therapy).

This research project first assessed the precision error of MR-FE derived stress, strain, and failure load outcomes at the proximal femur. With knowledge of precision errors, we then assessed relationships between upper-thigh muscle properties (muscle area, fat area) with MR-FE outcomes.

1.2 Scope

Chapter 2 provides a review of the current literature, focusing on the anatomy of the hip, fracture risk factors, clinical imaging techniques, FE modeling, and characterizing hip muscle properties. Chapter 3 outlines my research questions and project objectives. In Chapter 4, short-term *in vivo* precision errors of MR-FE outcomes at the proximal femur are reported. Chapter 5 explores the associations of muscle and adiposity with MR-FE failure loads. Chapter 6 includes an overview of the findings, details the research contributions, outlines the clinical significance, and offers suggestions for future research.

CHAPTER 2
LITERATURE REVIEW

2.1 Anatomy

2.1.1 Hip Joint

The hip joint acts as the structural link between the lower extremities and the axial skeleton, whereby it acts as a ball-and-socket joint consisting of the proximal femur and acetabulum [17]. The femoral head sits (acting as a ball) within the cup-shaped acetabulum (Figure 2-1), free to articulate while transmitting reaction forces and carrying the weight of the upper body. Contributing to the acetabulum structure are the ischium, ilium, and pubis pelvic bones. The ischium and ilium account for the majority of the pelvic structure, providing displacement boundaries to the femoral head [18].

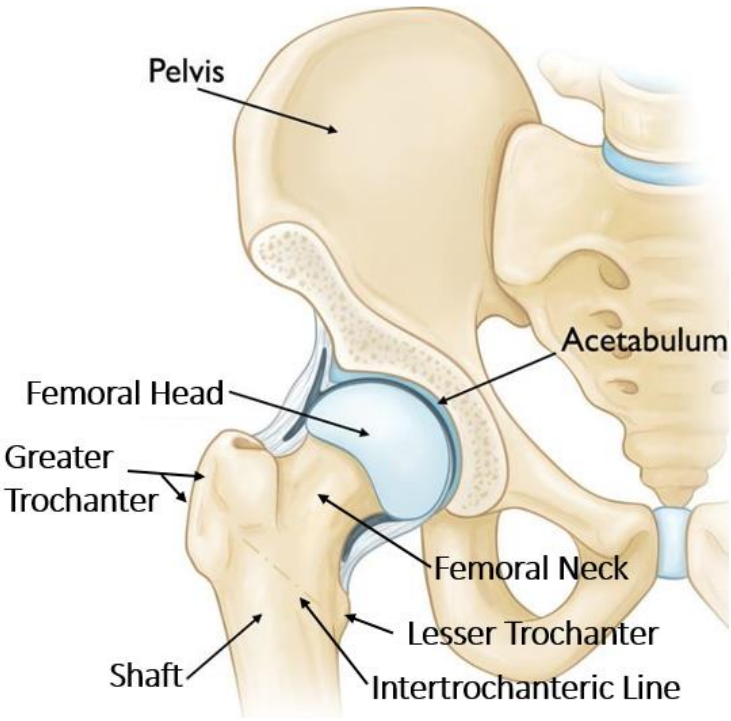

Figure 2-1. Anterior view of the hip joint, including the femoral head, acetabulum, greater trochanter, and lesser trochanter. Reproduced with permission from OrthoInfo © American Academy of Orthopedic Surgeons http://orthoinfo.aaos.org [19]

The femoral head is covered by a dense layer of articular hyaline cartilage except for an ovoid depression (fovea capitis femoris), which serves as the attachment point for the intracapsular ligament (ligamentum teres) [20]. Similarly, the acetabulum is covered in a "U" shaped articular cartilage, with a roughened depression (acetabular fossa) within the central region [21]. The inferior acetabular fossa contains a synovial covered fat-filled pad and also the attachment point of the ligamentum teres, both of which are critical in absorbing impact and assisting in an even distribution of forces around the joint [17,21,22].

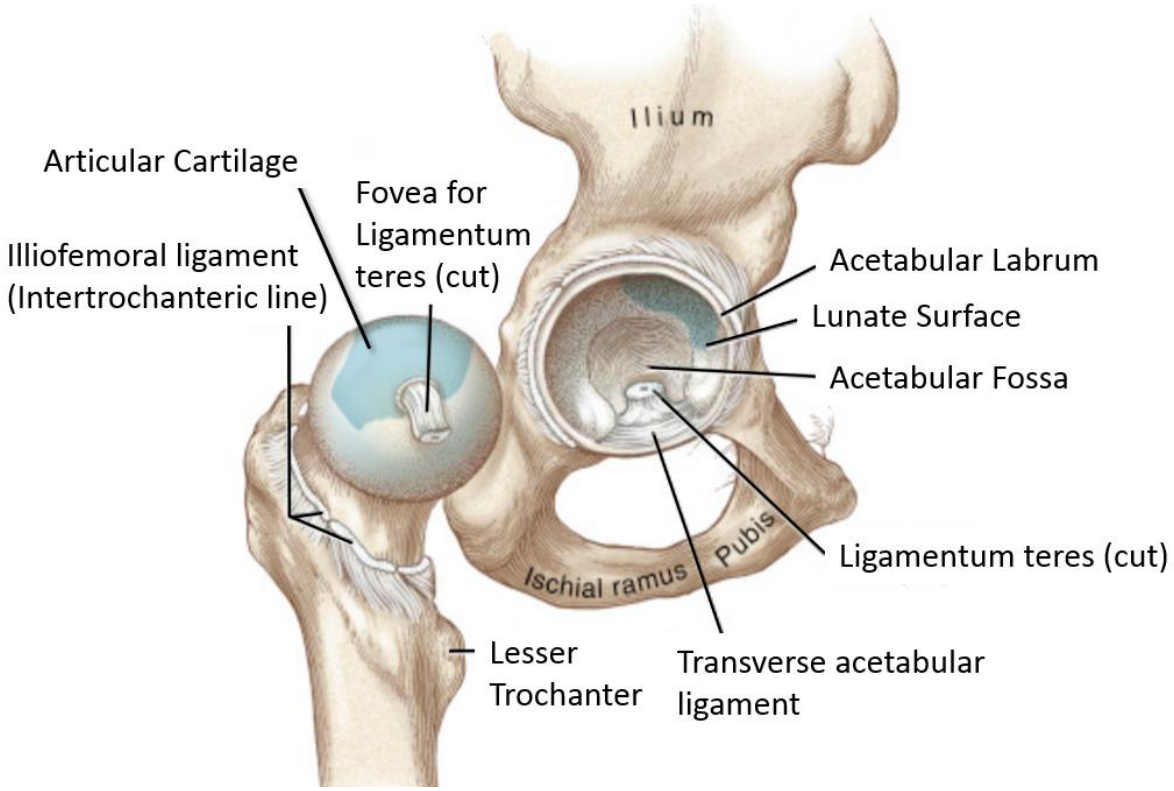

Figure 2-2. Labeled diagram of the right hip with internal components labelled. Regions of thickest articular cartilage are highlighted in blue. Modified from Mansfield et al., [23].

2.1.2 Proximal Femur

Anatomically, the proximal femur consists of five main components: the head, neck, greater trochanter, lesser trochanter, and shaft. The globular femoral head (caput femoris) is directed upward and medial-ward and is supported by the relatively thin structured femoral neck. The neck

(collum femoris) is a thin walled cylindrically shaped region that forms an (average) angle with the shaft of approximately 130° [24]. The femoral neck has the narrowest cross-section of the femur and is subjected to bending during loading [25,26]. Transitioning from the neck is the intertrochanteric region which resides between the greater and lesser trochanters (prominent processes). Situated on the lateral side of the femur, the greater trochanter serves as the insertion point of various muscles, including the obturator externus, obturator internus, superior gemellus, inferior gemellus, piriformis, gluteus medius, and gluteus minimus (Figure 2-3) [17,27]. The lesser trochanter is found below the neck on the posteromedial surface of the femur. The medial-most crest of the lesser trochanter serves as the insertion site for the psoas major muscle [17]. Located immediately below the lesser trochanter, the tubular femoral shaft is cylindrical in shape and extends downwards to the femoral condyles [27].

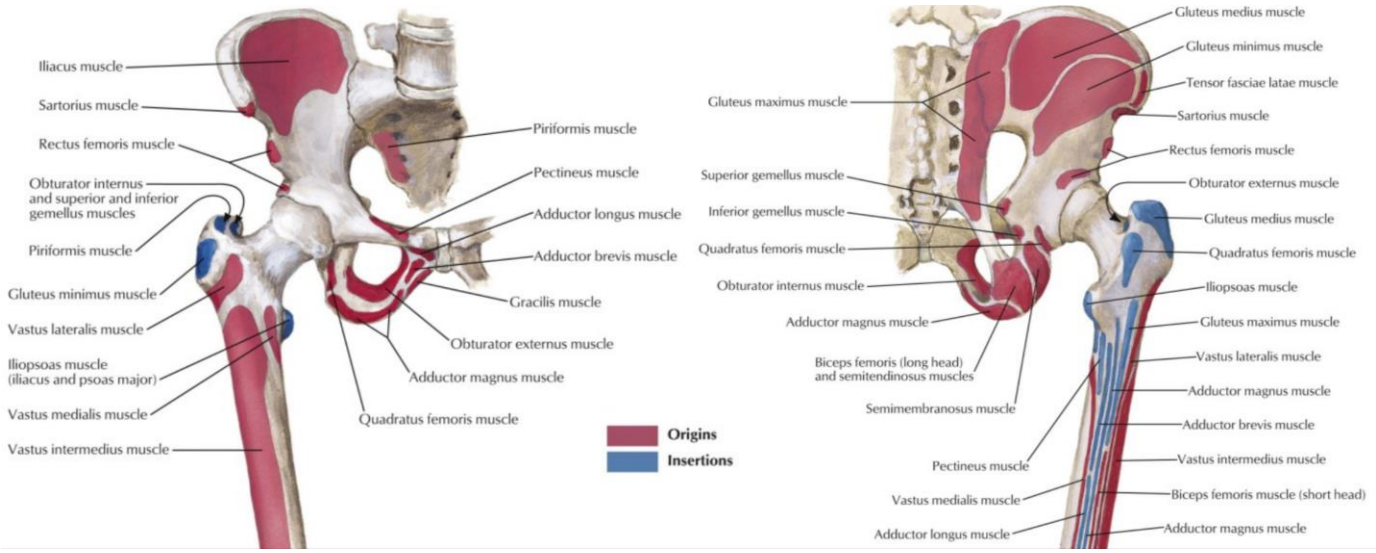

Figure 2-3. Muscle origin and insertion points of the proximal femur. Anterior view (left) and posterior view (right). Reproduced with permission from Frank et al., 2014 [17].

Bone is structurally complex, with geometrical and structural properties determining its behaviour under load. Macroscopically, human bone tissue can be classified as either cortical (compact) or trabecular (cancellous). Cortical bone is found primarily in the shaft of long bones

between the periosteal and endocortical surfaces and the outer shell around trabecular bone at proximal and distal ends of the bone. Cortical bone forms the hard, dense outer layer (cortex). Trabecular bone is highly vascularized, less dense, and is predominantly found at the ends of long bones surrounded by cortical tissue. Cancellous bone helps to reduce the weight of the skeleton, and provides support and protection for bone marrow cells [28]. Within the femoral head, neck, and trochanteric region, trabecular bone is surrounded by a thin cortical shell (Figure 2-4). Cortical thickness increases through the intertrochanteric region to the shaft, whereby it consists of a thick cortex surrounding marrow. Bone material is arranged to resist mechanical loading and avoid fracture, with each region of the proximal femur varying in structure in response to loading adaptation [29,30].

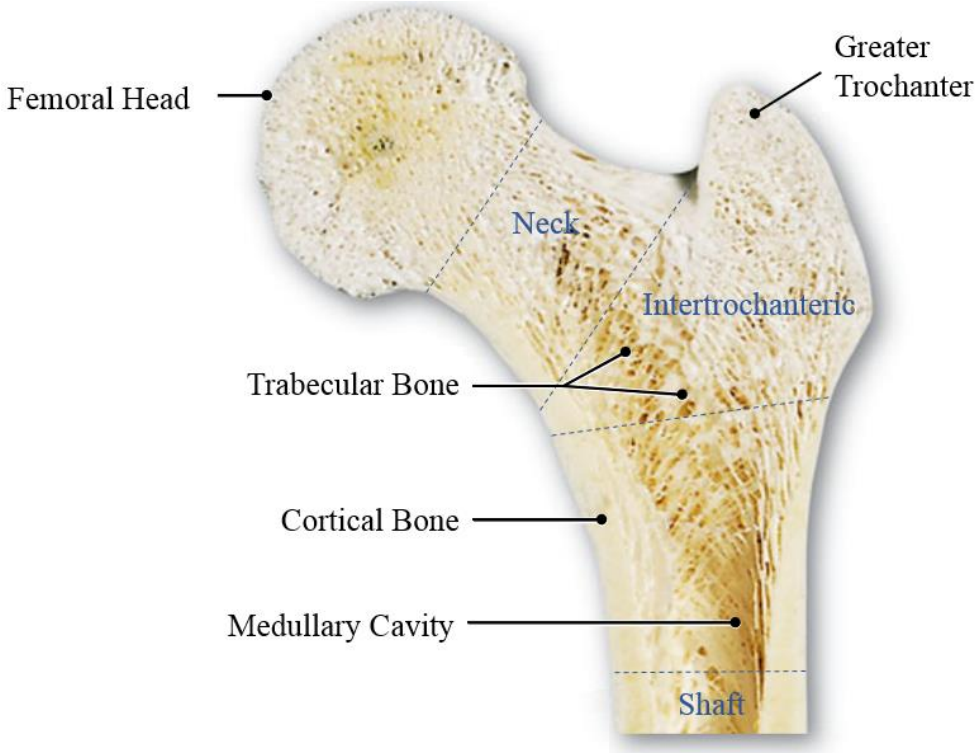

Figure 2-4. Internal structure of the proximal femur after sectioning. The distinguishable trabecula resides within the compact bone layer. Modified from Martini et al., [28].

2.1.3 Surrounding Muscles

Muscles are attached to bone through dense fibrous connective tissue (tendons and the entheses) and contribute to femoral loading through muscle-bone interactions [31]. To generate movement, large forces are generated and transmitted to the proximal femur to produce extension, flexion, adduction, abduction, and rotation by the muscles [32]. At the upper thigh surrounding the proximal shaft, there are four functional muscle groups which contribute to the movement and stability of the body. The muscle groups and the coinciding individual muscles are [33]:

- Hip extensors: gluteus maximus, semitendinosus, bicep femoris
- Hip adductors: adductor magnus, adductor longus, adductor brevis, gracilis
- Hip flexors: rectus femoris, sartorius
- Knee extensors: vastus intermedius, vastus medialis, vastus lateralis

Muscles at the hip may be infiltrated with adipose (fat) tissue which is a specialized connective tissue laden with adipocytes [34]. Surrounding the four individual muscle groups at the hip is intermuscular adipose tissue (InterMAT). Differing from InterMAT, intra-muscular adipose tissue (IntraMAT) is the fat infiltration between and/or within the muscle fibers [35]. Muscle to IntraMAT conversion occurs with age and is a predictive factor of metabolic disease, obesity, and muscle strength [34].

2.1.4 Loading

The proximal femur is designed to resist multiple loading conditions as it undergoes combined tension, compression, torsion, and bending during standard gait. Loads are distributed onto the femoral-head through the acetabulum. Cortical and trabecular bone plays a relative role in the load-carrying capacity of the proximal femur. Within the proximal femoral neck, the majority of load (independent of loading orientation) is supported through the trabecular bone; moving distally

toward the shaft, the load sharing reverses and the cortical bone takes the majority of the load [36]. The internal trabecular structure is arranged to provide an efficient manner for the internal strains to be resisted with the greatest efficiency as shown in Figure 2-5 [27]. During loading, the cortical bone is predominantly exposed to compressive loads that can induce micro damage. Bone fails due to the accumulation and growth of damage in the form of micro-cracks [37]. The proximal femur is thought to be highly adapted to the habitual loading orientation and less adapted to prevent fractures in the fall orientation [38].

Figure 2-5. Intact femur chemically cleared to show the orientation of the trabeculae, visible as curved bands, to resist loading [28]

2.2 Hip Fractures

Hip fractures are a serious injury, with an estimated 30,000 occurring annually in Canada [1]. Severe outcomes resulting from fracture include chronic disabling pain, depression, and mortality (elderly adults 65 years of age or older: 14-36% 1-year mortality rate) [2,39,40]. Following fracture, 50% of patients are unable to walk independently [41]. The decrease in physical independence results in approximately 25% of fracture victims remaining in long-term care facilities afterward [2]. Hip fractures within the neck and trochanteric regions create a high risk of

mortality by predisposing to circulatory disease, respiratory disease, and stroke [39,42]. As hip fracture risk increases with age, improved hip strength assessment tools and knowledge of bone and muscle interactions may help to negate serious outcomes.

Hip fractures are classified based on their failure location and occur primarily in the trochanteric, cervical (femoral neck), and shaft regions (Figure 2-6). Fractures predominately occur due to a sideways fall onto the greater trochanter originating from the standing position [2]. Although substantially less common, stance fractures may occur in adults due to above average habitual loading (e.g. axial loading fall, car accident) [43]. The proximal femur is primarily adapted to withstand loading in the habitually weight-bearing direction. As such, for 98% of hip fracture patients, the fracture was the result of a sideways fall and not due to stance loading [43,44].

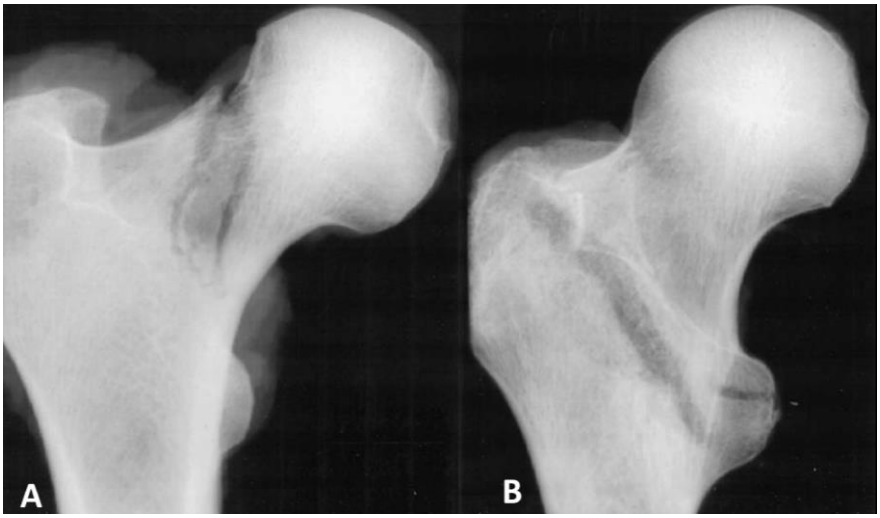

Figure 2-6. Radiographs of proximal femur fractures. Neck fracture from stance loading (A); Intertrochanteric fracture from a sideways fall (B). Modified from Keyak et al. [45]

Typically, intertrochanteric fractures occur from a sideways fall and femoral neck fractures occur from stance loading [38,46]. Within the proximal femur, the neck is generally considered the weakest site due to its small cross-sectional area and thin cortical wall thickness (Figure 2-4). During standard gait, the greatest strains typically occur in the thick, habitually-adapted

inferomedial neck region. For a sideways fall onto the greater trochanter, the state is reversed, with maximum compressive strains occurring in the thin superolateral neck and the lower tensile strains occurring in the thick inferomedial neck [47,48]. A summary of experimental fracture loads for stance and sideways fall configurations can be found in Table 2-1.

Table 2-1. Summary of experimental hip fracture failure loads from previous studies simulating sideways fall and stance loading configurations

Orientation	Study (ref. #)	Number of Specimens	Sex	Mean Age (SD)	Mean Fracture Load (SD) [N]
Sideway fall	[49]	33	NR	81.1 (6.7)	3892 (910)
	[50]	10	4F, 6M	73.8 (7.1)	4032 (1814)
	[50]	10	3F,7M	31.7 (12.5)	7980 (1571)
	[38]	12	6F,6M	84.0 (5.3)	4032 (370)
Stance	[51]	17	10F,7M	70 (~10)	8500 (~1525)
	[52]	40	24F,16M	82 (12)	9031 (3444)

2.2.1 Risk factors

A wide variety of factors have been found to influence hip fracture risk, with bone morphology, muscle strength, sex, and age being highly influential [2,53]. In North America, the risk of fracturing a hip at age 50 is 6% and 17% for men and women, respectively, with fracture likelihood increasing with age [2]. Less-influential risk factors linked to fracture risk include ethnicity, nutrition, alcohol consumption, drug intake, and disease [4,20]. Although these factors have been found to play a role in hip strength, this thesis will focus exclusively on bone morphology and muscle/adiposity measures.

Clinically, bone strength is a general term used to refer to bone's ability to resist loading, be it in terms of deformation or failure, with a high bone strength suggesting a reduced fracture risk. Osteoporosis is a skeletal disorder characterized by low bone strength and microstructural deterioration of bone predisposing to an increased risk of fracture [4]. Morphologically, people

typically experience cortical thinning and overall bone loss with age as skeletal loading demands decrease, which increases susceptibility to failure [29]. In comparison to healthy bone, osteoporotic bone has reduced strength, stiffness, and ability to absorb energy before failure [54]. Importantly, advanced imaging techniques can improve estimation of fracture risk [55], and facilitate research into preventing osteoporotic fractures.

Typically the greatest forces applied to the proximal femur are due to muscular contractions and gravitational loading (body weight) [16,56]. Muscle cross-sectional area is a surrogate measure of muscle force and is used to describe the applied muscular loads onto the femur [57,58]. Muscle forces contribute to balance and help to prevent dangerous hip fractures as a result of a sideways falls onto the greater trochanter. With aging, an individual experiences a loss of muscle mass and infiltration of muscle tissue by fatty lipids, increasing the risk of a fall inducing fracture [59]. In addition to muscle area measures, Addison et al., found that increased IntraMAT in the proximal hip muscles was positively associated with increased gait variability and poorer balance [60]. In the mechanostat model, it is suggested that bone is a biomechanically-regulated structure that is primarily dominated by physical activity and muscle loading [12]. Functionally, the model suggests that bone modulates its structure to meet loading demands and eliminate unnecessary mass [13,56]. Research suggests that muscle and bone strength are inherently related and that insufficient muscle force leads to inadequate bone strength and fragility [12,56]. It is currently unclear which muscle groups and properties (pure muscle, adiposity) are most closely associated with proximal femoral bone strength

2.3 Current Methods for Estimating Proximal Femoral Strength

2.3.1 Mechanical Testing

The proximal femur's strength can only be directly determined using destructive mechanical testing. *Ex vivo* studies have quantified femoral strength using simple compression tests in either a stance or fall configuration [49–51,61]. As such, non-invasive imaging modalities and loading are critical to evaluate bone strength *in vivo.*

2.3.2 Imaging

2.3.2.1 Dual Energy X-Ray Absorptiometry

Dual-energy X-ray absorptiometry is the current clinical *in vivo* standard for evaluating osteoporosis and fracture risk via aBMD (g/cm^2) measurements at the proximal femur [62]. DXA is a 2D projection-based imaging tool that consists of two x-ray beams with different energy levels passing through the region of interest in the body. Making use of the differential absorption (attenuation) of bone and soft tissue, pixels within a region are averaged to obtain aBMD. This measure is considered the gold standard in assessing bone strength, with a low aBMD value associated with increased risk of fracture at the population level [63]. People are identified as at risk for fracture (or osteoporotic) if their aBMD lies at least 2.5 standard deviations below the average aBMD for a young healthy adult person (T-score <2.5) [6].

A major limitation of DXA is the inability to account for complex 3D geometry of the hip using a 2D scan. Additionally, aBMD measures cannot individually distinguish cortical and trabecular bone [64]. Although low aBMD is an indicator of hip fracture risk, studies have found that it is insufficient in fully characterizing hip strength due to these substantial limitations [8]. A study by Schott et al., found that only 48% of hip fracture patients are identified as at risk of

fracture through a DXA scan [9]. Similarly, most patients who suffer an osteoporotic hip fracture are misclassified as non-osteoporotic by DXA [65].

To address the limitations of DXA, the Hip Strength Analysis (HSA) application was developed to incorporate geometric contributions of bone strength. In addition to aBMD, HSA computes the bone cross-sectional area, cross-sectional moment of inertia, section modulus, buckling ratio, and cortical thickness at the femoral neck (narrowest cross-section) and shaft (~2cm below the lesser trochanter) [64]. To extract geometry from a DXA scan, a line of pixels along the region of interest (in the coronal plane) is converted into an "equivalent bone surface area" by assuming that bone is uniformly distributed and forms a circular cross-section [66]. When compared to aBMD, HSA outcomes have shown a modestly improved ability to predict bone failure (R^2 = 43%) [66,67]. A major limitation of HSA is the frequent overestimate of geometry (and strength) due to a noisy image [66]. It has also been found that small rotation changes of the proximal femur have a large effect on projected dimensions with an *in vivo* measurement error (i.e., precision error) >10%, assessed via the root mean square coefficient of variations ($CV\%_{RMS}$) [68]. Importantly, low precision errors are essential for ensuring that imaging measures are trustworthy and for assessing the validity of statistically significant differences (i.e., a difference may exist in a statistical sense, but if the difference is comparable to the measurement error, the difference cannot be trusted). Altogether, although HSA offers strength-characterizing bone metrics, the method may be regarded as somewhat imprecise and insufficient, primarily as it relies on 2D data to describe 3D geometry.

2.3.2.2 Computed Tomography

Computed Tomography (CT) is a 3D x-ray based technique which has similarly been used to evaluate femoral bone strength. Image acquisition occurs through a series of thin radiographic

"slices" over a variety of angular positions around the object followed by reconstruction [55]. Reference phantoms are used to convert CT acquired Hounsfield units (HU) to an equivalent volumetric bone mineral density (vBMD or BMD, mg/cm^3). BMD is near equivalent to ash density (ρ_{ash}), which is related to apparent density (ρ_{app}) by a ratio of 0.55 [69]. CT offers numerous clinical advantages over DXA as CT measurements are less influenced by positioning and size [70]. Additional advantages of CT include the ability for 3D geometric measurements, and capability to distinguish between cortical and trabecular bone [55]. Applications of CT are readily studied due to rapid scanning time and general availability [71].

To date, CT has been applied to investigate proximal femoral strength and muscle properties using FE modeling and morphological bone strength metrics [45,60]. Similar to DXA-based HSA, CT has been used to compute metrics such as the cross-sectional area, cross-sectional moment of inertia, section modulus, buckling ratio, and cortical thickness at the femoral neck [72,73]. CT-obtained bone strength metrics have an *in vivo* measurement error (i.e., precision error) <7.3%, assessed via the root mean square coefficient of variations ($CV\%_{RMS}$) [74].

A major drawback of CT is the exposure of harmful ionizing radiation (3.1-4.9 mSv) to the radiosensitive organs in the pelvis which is much higher than the effective dosage that a DXA scan (0.009 mSv) delivers [75–77]. CT based studies of the hip have predominantly focused on elderly adult populations due to radiation exposure. Additionally, CT offers an inferior soft tissue contrast, and poorer imaging quality with the presence of metal, limiting the application of CT towards muscle-based studies [78].

2.3.2.3 Magnetic Resonance Imaging

Magnetic resonance imaging is a noninvasive 3D technique which is primarily used to image soft tissue (e.g., cartilage, ligaments, muscle). MRI is well-suited towards the application of imaging

the pelvis as it does not emit harmful ionizing radiation to the participant. In MR imaging, atomic nuclei (water, hydrogen protons) are aligned using a powerful permanent magnetic field. Radio frequency pulses are applied at the resonance frequency of hydrogen to alter the magnetization alignment of the protons. Afterwards, the magnetic field "relaxes" and realigns, inducing a detectable RF pulse which is constructed into an image [79].

MRI is a highly effective modality for imaging muscle and fat due to its superior soft tissue contrast [80]. Previous research has identified MRI as the gold standard in quantifying IntraMAT for its high sensitivity to early fat infiltration [35,81]. In a few previous studies, MRI has been used to measure bone geometry, estimate bone strength, differentiate cortical and trabecular bone, and assess muscle cross-sections (Figure 2-7) [33,82,83].

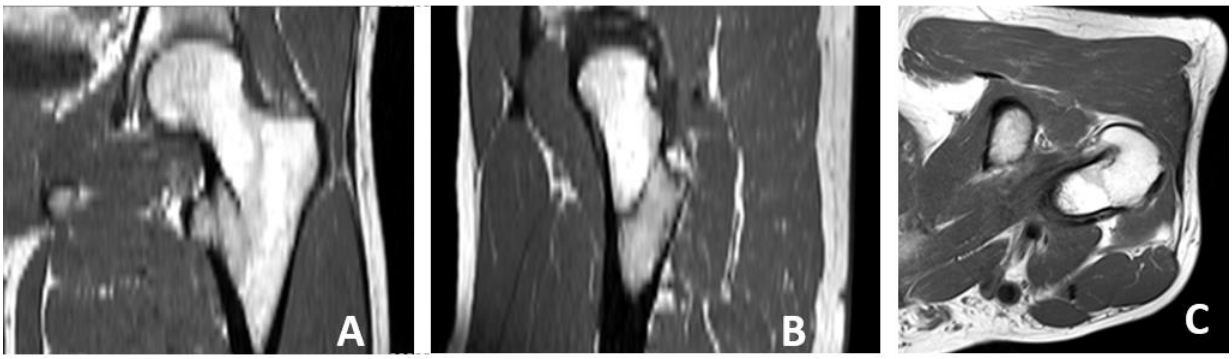

Figure 2-7. MRI scan of the left proximal femur (cubic interpolated). Coronal view (A), Sagittal view (B), and Transverse view (C)

Relevant to this research, MR has been previously used for hip bone strength studies and is suitably capable of extracting structural details pertaining to the cortical and trabecular architecture of bone [83]. MRI-based morphological measures of bone and muscle traits at the femoral neck and shaft have demonstrated an *in vivo* precision errors < 7.1% [33]. MRI does not directly image bone, but rather the high intensity tissues surrounding bone (e.g., fatty marrow, water). This is because bone shows no signal with MRI as it is primarily composed of calcium hydroxyapatite, which has one proton that does not move. Therefore, the decay time of bone is

very short and minimal signal arises. By measuring fluid intensity, indirect measures of bone quantity can be obtained using MRI [84]. As such, differing from CT, MRI provides a negative contrast of mineralized tissue in which cortical bone has a low intensity, and fat a high intensity. MRI can assess the volume of mineralized bone per unit volume, which is known as the bone volume fraction (BVF). With the assumption that the material density of compact bone is 1.8 g/cm^3, the BVF is related to the apparent density using ρ_{app} = 1.8*BVF [85].

Growing recognition that femoral strength is dependent on bone material properties and distribution has led to research on morphological based bone strength metrics at the femoral neck and shaft. Previous studies have focused on metrics for their simple ability to estimate the hip's ability to resist failure [33,86,87]. Metrics encompassing different modes of strength are highly relevant as the proximal femur experiences tension, compression, bending, and torsion during loading [88]. It has been previously found that image-based bone strength metrics (total cross-sectional area, cortical cross-sectional area, area moment of inertia, section modulus) are associated with failure load obtained via mechanical testing ($r^2 \geq 0.46$) [89]. Although morphological metrics provide a method of assessing hip strength, they do not consider the entire proximal femur, providing an opportunity for improved strength characterization.

Due to signal-to-noise limitations which negatively affect the resolution of a scan, MRI research studies focused on the proximal femur are relatively less studied than peripheral bone sites (distal radius, tibia, and ankle). Noise is a particular issue with imaging of the hip due to the inability to place an MR coil (basically an enhancing device to primarily detect MR signal, some are transmit/receive) close to the proximal femur as a result of the large amount of surrounding soft tissue (unlike peripheral sites) [90]. Additional limitations of MR imaging include high operating costs and long acquisition scan times which increase the potential for motion artifacts

[79]. Intensity inhomogeneity, commonly referred to as “bias field”, is common in MRI scans and distorts pixel intensities, limiting the quality of a scan and affecting image analysis. Methods such as segmentation and registration are highly sensitive to the variations in image intensity caused by a bias field [91]. Bias field has no anatomical relevance and can be caused by a variety of factors including:

- Non-uniformity in the radio-frequency coil (RF) [92,93]
- Non-uniform static field [94]
- Size and electromagnetic properties of the imaged object [93,95]

Correction algorithms have been previously developed which assume that the bias field is a smoothly varying multiplicative field. Amongst retrospective correction methods available, the open source N4ITK nonparametric non-uniform normalization algorithm is considered the most effective and has been used for various research applications [78,96]. The correction works by iteratively determining the intensity non-uniformity on a per-pixel basis and then applies a smooth multiplicative surface over the original scan, as shown in Figure 2-8.

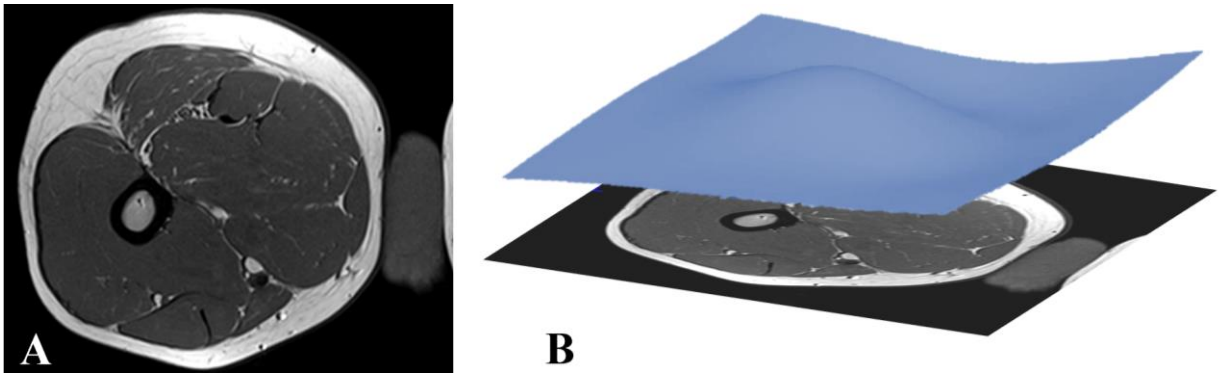

Figure 2-8. MRI slice of the femoral shaft exhibiting inhomogeneity (A); Bias field multiplicative correction applied as a surface over the original MR image (B).

2.3.3 Finite Element Modeling

Subject-specific finite element modeling is a non-invasive numerical technique that can be used to describe bone strength *in vivo*. Unlike morphologically based strength metrics and aBMD measures, FE models can consider the strength of the entire proximal femur by accounting for geometry as well as bone material tissue properties and their distribution. FE modeling is based on dividing a complex object into small finite elements of simple geometry, whereby deformation and stresses can be easily calculated [97]. FE modeling has been used to study human soft tissue and bone previously using various imaging modalities such as CT and MRI, though predominantly CT [82,98,99]. FE modeling is superior to gold-standard aBMD and morphological strength metrics to estimate bone strength as it can incorporate variations in architecture and mechanical tissue properties [100]. Predicted failure load is important for strength characterization as Samelson et al. found strong associations between peripheral-QCT predicted distal tibia failure loads and incident fracture (Cox proportional hazard regression models to calculate hazard ratios: 2.40, 95% confidence interval) [101].

For *in vivo* FE studies, bone strength is widely reported as the estimated failure load [100]. Previous FE studies have reported the estimated failure load as the force magnitude to cause either a fixed percentage (e.g., 5%) of elements or a fixed volume (e.g., 150 – 450 mm^3) to fail [99,102]. Edwards at al. looked at the absolute percent error between experimental and predicted distal radius failure loads of different fixed volumes (150 mm^3 - 450 mm^3) and found that for a tensile to compressive strength ratio of 0.75, the error was lowest (<30%) with a 150 mm^3 volume [99]. A similar study but of the proximal femur found a strong correlation between predicted and experimental failure loads ($R^2 = 0.94$, $p < 0.0001$); however, they noted that ductile yielding of a proportion of bone tissue (1.5% to 6.4%) led to the initial structural failure instead of a fixed

volume [102]. Currently, the measurement repeatability of linear MR-FE mechanical outcomes have not been reported at critical failure regions for fall and stance loading configurations.

2.3.3.1 Computed Tomography

CT is the primary imaging modality which has been used for FE modeling of the proximal femur and other sites. Typically, a quantitative reference phantom is included in CT images, allowing estimates of BMD. This technique is typically referred to as QCT-FE. Relevant to this research, key FE studies by Keyak et al., predicted fracture location and failure load of the proximal femur, with validation by experimental testing [45,98,103,104]. These studies modeled fall and stance loading configurations and provided the framework for orientation and boundary conditions used in the majority of subsequent research studies [82,105–107]. Regression results have shown 19% unexplained variance between stance and fall failure loads, indicating that the results from one loading configuration are not indicative of those in another loading configuration [51]. It is currently unknown which loading configuration is best suited for characterizing fracture risk. As such, FE studies of the proximal femur predominantly model both the stance and fall loading orientations.

Studies performed *in vivo* and *ex vivo* have validated the accuracy of QCT-FE studies in estimating femoral strength using various failure theories (e.g., von Mises, Brittle Coloumb Mohr) [103,108,109]. Relatedly, CT-FE studies provide a better prediction of femoral strength than DXA-based methods [110]. Major CT-FE studies for the fall and stance configuration are summarized in Table 2-2.

Table 2-2. Summary of key CT-FE hip studies looking at stance and fall loading configurations

Study (ref. #)	Subjects/ Specimens	Sex	Mean age (SD)	Configuration	Scanning	Precision Errors	Findings
[104]	18	M & F	70.3 (NR)	Stance and Fall	*ex vivo*	Not reported	Strong relationship between experimental and measured fracture load for fall (R^2 = 0.90) and stance (R^2 = 0.76) loading using distortion energy theory and Brittle Coulomb Mohr (BCM).
[110]	51	M & F	67.5 (NR)	Stance	*ex vivo*	Not reported	FE models with hexahedral elements explained 84% variance in strength whereas DXA explained 66%.
[45]	18	M & F	70.3 (NR)	Stance and Fall	*ex vivo*	Not reported	Nonlinear FE models predicted fracture location with accuracy for fall and stance (R^2 = 93%).
[107]	10	F	75.1 (NR)	Stance and Fall	*in vivo*	Not reported	Predicted failure load in patients with contralateral hip fractures were smaller in comparison to healthy participants. Predicted fracture loads for the fracture (mean: 2525, SD: 579 N) and control (mean: 5291, SD: 803 N) groups varied for the stance configuration. Predicted fracture loads for the fracture (mean: 1825, SD: 387 N) and control (mean: 4858, SD: 880 N) groups varied for the fall configuration.

[102]	12	M & F	76 (10)	Fall	*ex vivo*	Not reported	Trabecular failure occurred before cortical bone. A small proportion of bone (1.5% to 6.4%) led to total structural failure of the femur
[108]	14	M & F	77 (NR)	Stance and Fall	*ex vivo*	Not reported	FE-predicted and measured failure loads were highly correlated (R^2 = 0.89) when using a principal strain criterion and a non-linear modeling approach.
[109]	100	F	75 (9)	Stance and Fall	*in vivo*	Not reported	Loading orientation of the proximal femur affected the accuracy of the FE outcomes.
[111]	10	M & F	55.6 (3)	Stance	*in vivo*	$CV\%_{RMS}$= 1.9% DOF = 10	Reported the short-term precision of femoral failure load using the approach by Glüer. Failure load was estimated using a previously obtained correlation with FE derivied stiffness (R^2 = 0.92). Study did not meet the conservative recommendation of 28 degrees-of-freedom (DOF) [112].
[113]	4	F	68 (3)	Stance and Fall	*ex vivo*	Not reported	Agreement between the predicted effective von Mises stress failure load and experimental results (14% normalized error). Poor agreement between measured and predicted principal strains (22%)

2.3.3.2 Magnetic Resonance Imaging

Subject-specific FE modeling using MRI (referred to as MR-FE) is a safe and powerful technique to assess hip strength *in vivo.* MR imaging of the femur, in combination with FE modeling, can be used to assess strength through considerations of bone geometry and quantity, non-invasively [114]. In a review of femoral FE studies, fewer studies have used MRI than CT, likely due to limitations in signal-to-noise ratios which may distort pixel intensities and the relative limited resolution. However, as noted earlier, MR offers non-ionizing multi-planar 3D images of bone and muscle. Accordingly, MR-FE is an emerging method for assessing hip strength that is gaining interest, specifically due to avoidance of ionization radiation. MR-FE modeling of the proximal femur has been predominantly conducted by research groups led by Chang, Sievänen, and Rajapaske [82,105,115,116].

Like CT, MR-based modeling can be used to look at various mechanical outcomes such as stress, strain, failure load and stiffness which describe hip strength. In two complementary studies, Abe et al., developed linear FE models of the proximal femur and compared the mean von Mises stress and failure loads of competitive athletes with different loading histories. Results from the studies indicated that MR-FE derived measures of von Mises stress and failure load differentiated groups (mean von Mises stress: -9 to -32%, failure loads: +11 to +26%) [82,105]. To date, there has only been one study which assessed the *in vivo* precision error of MR-FE; however, the study only evaluated the whole-bone stiffness, and elastic modulus for a small region of interest (ROI) using non-linear micro MR-FE models [116]. Currently, the measurement repeatability of linear MR-FE mechanical outcomes has not been reported at critical failure regions for fall and stance loading configurations. A summary of MR-FE studies is found in Table 2-3.

Table 2-3. Summary of key MR-FE hip studies looking at stance and fall loading configurations

Study (ref. #)	Subjects/ Specimens	Sex	Mean age (SD)	Configuration	Scanning	Precision Errors	Findings
[114]	44	F	68 (10)	Stance & Fall	3T MRI *in vivo*	Not Studied	Previously fractured femurs have lower bone strength than controls (up to 67%) in the neck and intertrochanteric regions
[116]	12	M & F	57.4 (14)	**Fall	3T MRI *in vivo*	*$CV\%_{RMS}$ < 6.6% DOF = 12	Assessed the whole-bone stiffness, and the elastic modulus for a 10 x 10 x 10 mm^3 microarchitecture region of interest (ROI) in the neck. Study did not meet the conservative recommendation of 28 degrees-of-freedom (DOF) [112].
[105]	111	F	24.7 (6)	Fall	1.5T MRI *in vivo*	Not Studied	Lower mean von Mises stress (-10 to -23%, p <0.05) in the femoral neck of female adult athletes than non-competitively active participants
[117]	20	F	62.5 (8)	Stance & Fall	3T MRI *in vivo*	Not Studied	Stance loading FE outcomes are not predictive of fall loading outcomes and should be assessed independently

[82]	111	F	24.7 (6)	Fall	1.5T MRI *in vivo*	Not Studied	Higher fracture loads (+10 to +26%, p <0.05) in the femoral neck of adult athletes than non-competitively active women. Fall fracture loads from 2.1- 4.4 kN

* $CV\%_{RMS}$ = Root-mean squared coefficient of variation, expressed as a percentage

** Modified fall configuration. Applied a 1% strain to the femoral head

2.3.3.3 Modeling Approaches

The FE modeling approaches which are used in the literature vary based on the research objectives. Generally for femoral FE studies, standard linear FE models are used due to their modest computational demand and imaging resolution constraints. Table 2-4 contains a summary of common CT-FE and MR-FE modeling approaches.

Table 2-4. Common FE modeling approaches

Approach	Description	Attributes
Standard FE	Subdivision of an image into non-overlapping components of simple geometry called elements (mathematical model).	• Appropriate element size is established using mesh convergence
Micro-FE	FE voxels are directly derived from equally shaped/sized image voxels, and are on the length scale of micrometers.	• Typically used to model individual trabeculae [116,118]
Linear FE	Consisting of infinitesimal deformation (geometric linearity) and linear stress-strain relations.	• Small computational demand • Limited to modeling the onset of failure
Non-Linear FE	Consisting of large deformations (geometric nonlinearity) and may result in nonlinear stress-strain relations.	• Large computational demand • Can model post yielding

To avoid partial volume effects and surface smoothening, which may inhibit cortical detail, 8-noded hexahedral (brick) elements have been used in all previous MR-FE modeling studies to date [10,82,105,117]. Conversely, when using tetrahedral elements, this requires intensive surface smoothing and careful strategies to map elastic modulus to elements.

2.3.4 Bone Material Properties

In MR-FE modeling, differences in pixel intensity between bone, fat, marrow, and muscle are fundamental parameters used for segmentation and deriving material properties. Bone volume fraction (BVF) is the volume of mineralized bone per unit volume, and can be calculated from a grayscale MRI scan in which the pixel intensity represents the fractional occupancy of bone [83]. BVF and BMD are strongly related (R^2 =0.8) and used somewhat interchangeably as they both describe the bone mineralization and porosity, expressed as either a density or fraction [11]. By measuring the intensity of the fat surrounding the proximal femur, indirect measures of bone quantity (BVF) can be obtained using MRI [84]. Hwang and Wehrli found that voxel-specific BVF's can be computed using the pixel intensity (Int_{voxel}) and the maximum fat intensity (Int_{max}) in the MRI scan as follows [11]:

$$\text{BVF} = 1 - \frac{Int_{voxel}}{Int_{max}} \tag{2-1}$$

As bone material properties must be estimated using MRI, there are two common approaches used to assign voxel specific elastic moduli (*E*):

i. Bone is assigned a constant elastic modulus for cortical and trabecular bone [102,105]
ii. Elastic moduli are estimated from the BVF using previously found relationships derived from experimental testing [10,114,117,118]

In contrast with the constant elastic modulus approach, the BVF derived elastic moduli approach has been used for MR-FE studies due to its ability to more accurately represent the material properties of the hip, as well as account for material properties distribution [115]. The relationships which are used to estimate bone mechanical properties from the scan are based on experimental testing and are dependent on the cadaveric specimens used. As such, it is important

to use relationships derived from similar anatomical locations and specimen age being studied. Interestingly, Öhman et al., presented a proximal femoral elastic modulus-ash density relationship which proved to be valid for all ages ($R^2 = 0.86$, $p < 0.001$) as shown in Figure 2-9. This study also showed that bone failed in compression with an approximate strain of 10,000 μstrain and was not dependent upon density [119].

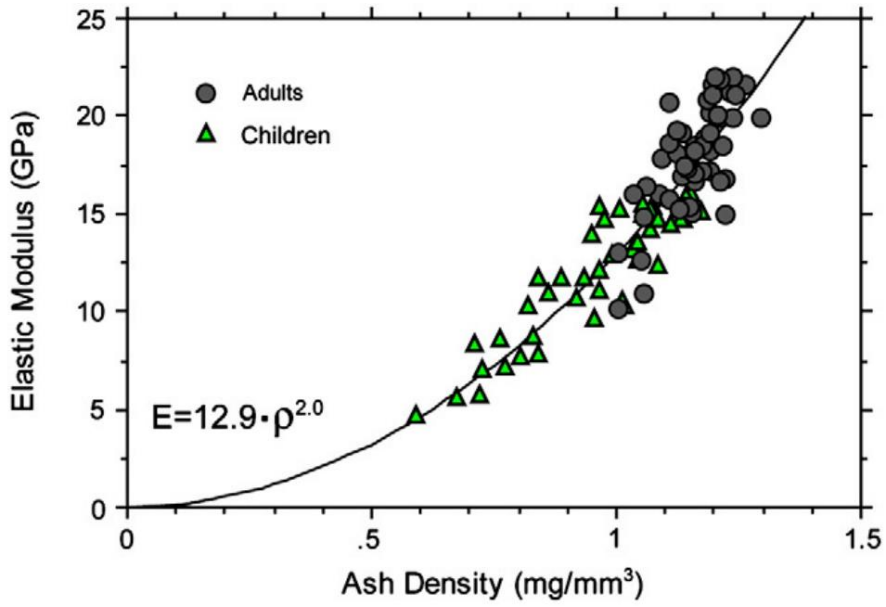

Figure 2-9. Plot of the elastic modulus-ash density relationship. The line represents a power model ($y=mx^b$) with the equation shown [119].

To estimate the elastic modulus of each voxel, the BVF, apparent density (ρ_{app}), and ash density (ρ_{ash}) are related using previously found relationships by Gibson et al. and Keyak et al [69]. Combining known relationships, the elastic moduli are ultimately computed from the image intensity [119], with a summary of studies and previously used relationships shown in Table 2-5.

Table 2-5. Previously published relationships which can be used to relate voxel-specific BVF to the elastic modulus of cortical and trabecular bone

Study (ref. #)	Equation	Units
[85]	$\rho_{app} = 1.8 * \text{BVF}$	g/cm^3
[120]	$\rho_{ash} = 0.6 * \rho_{app}$	g/cm^3
[119]	$E = 12.9 * \rho_{ash}^2$	GPa

Combining the previously published relationships (Table 2-5) and equation 2-1, the voxel specific elastic moduli can be assigned based on the image intensity using the equation:

$$E = 12.9\left[1.08\left(1 - \frac{Int_{voxel}}{Int_{max}}\right)\right]^2 \quad (2\text{-}2)$$

The E used in the above equation pertains to E_3, the principal compressive direction. Although bone is an orthotropic material, it is typically modeled as isotropic as various validation studies have shown no marked improvement in explained variance when accounting for anisotropy [121].

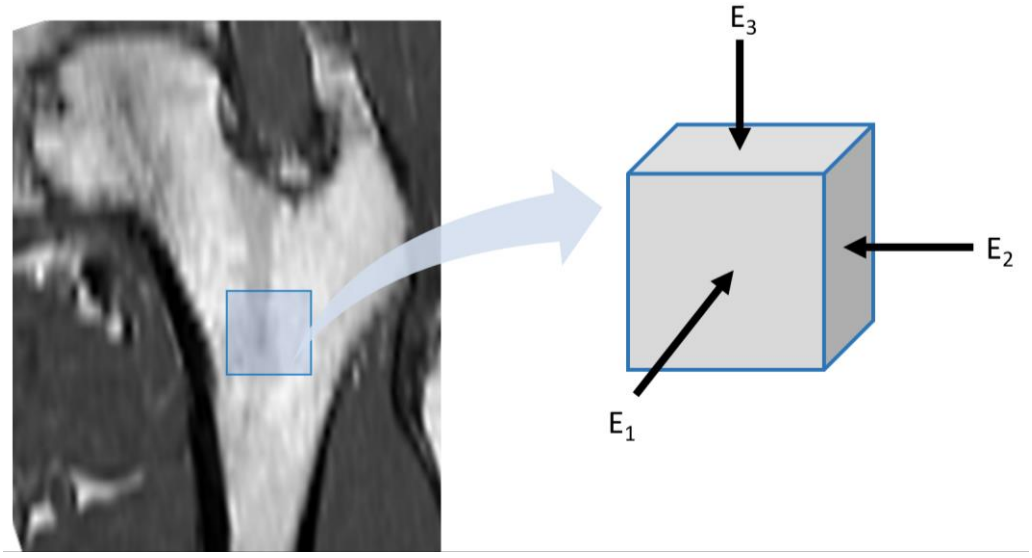

Figure 2-10. Principal directions of the material. The elastic modulus relationship presented in Equation 2-2 pertains to E_3 as per Ohman et al [119].

2.3.5 Failure Criteria

Experimental studies have found that bone fails around a specific strain. As per Morgan et al., the yield strain of femoral bone in tension is approximately 7000 μstrain [122], and 10000 μstrain for cortical bone [119]. Unlike yield strains which are considered constant for cortical and trabecular bone, the yield stress varies with elastic modulus [122]. With this knowledge that bone fails by strain, we can either assess failure if strain reaches these limits, or multiply these strain values by individual elastic moduli to find stress limits for individual elements [99]. Both approaches assume that bone failure is strain-driven but apply different approaches. With established failure strain-driven limits, failure theories can be applied to predict the failure load using FE.

It is currently unclear which failure criterion is optimal for predicting *in vivo* bone strength. Three prior CT studies (one distal radius and two proximal femora) have assessed explained variance in predicted experimental failure loads with various strain-driven failure theories; however, the outcomes of the studies were contradictory [99,103,113]. Keyak et al. found that the strain failure criteria (von Mises Strain and normal principal) were less accurate than stress-based criteria (von Mises Stress and brittle Coloumb Mohr) [103]. Edwards et al. found the best accuracy with the stress-based brittle Coulomb-Mohr theory in comparison to other stress/strain criteria with a tensile-compressive strength ratio of 0.7 [99]. Additionally, Lotz et al. found that the von Mises strain criterion provided the most accurate bone failure load prediction [113]. It remains unclear which failure criterion is best suited, specifically in terms of precision, for estimating hip strength. Precision of a specific failure theory is important as it may return good predictions of hip strength yet have high variability (poor precision). Of potential relevance to this research, the findings of the comparative study by Keyak et al. and Lotz et al. were obtained using large hexahedral

elements (3 mm x 3 mm x 3 mm), whereas Edwards et al. used smaller elements (nominal size of 1 mm^3) with a voxel size of (234 μm x 234 μm x 625 μm) [99,103,113].

2.3.5.1 von Mises Stress Failure Theory (Distortion Energy)

The von Mises stress failure theory assumes that failure occurs when the distortion (deviatoric) energy per unit volume for a general stress state reaches or exceeds the distortion energy for a uniaxial test (critical limit). As bone is weaker in tension than compression, the tensile strength (σ_{yt}) component is only considered (calculated from local E and σ_{yt}). The equivalent, or effective stress is known as the von Mises stress (σ_{vm}) and is calculated from the principal stresses (σ_1, σ_2, and σ_3) [123]. The safety factor (n) using the von Mises stress failure theory is found using

$$n = \frac{\sigma_{yt}}{\sigma_{vm}} \tag{2-3}$$

where the von Mises stress is calculated from

$$\sigma_{vm} = \left[\frac{(\sigma_1 - \sigma_2)^2 + (\sigma_2 - \sigma_3)^2 + (\sigma_3 - \sigma_1)^2}{2}\right]^{\frac{1}{2}} \tag{2-4}$$

2.3.5.2 von Mises Strain Failure Theory

The von Mises strain failure theory assumes that failure occurs when the distortion (deviatoric) energy per unit volume for a general strain state reaches or exceeds the distortion energy for a uniaxial test (critical limit). Only the weaker tensile yield strain (ε_{yt}) is considered. The equivalent, or effective strain is known as the von Mises strain (ε_{vm}) and is calculated from the principal strains (ε_1, ε_2, and ε_3). The safety factor (n) using the von Mises strain failure theory is found using

$$n = \frac{\varepsilon_{yt}}{\varepsilon_{vm}} \tag{2-5}$$

where the von Mises strain is calculated from

$$\varepsilon_{vm} = \left[\frac{(\varepsilon_1 - \varepsilon_2)^2 + (\varepsilon_2 - \varepsilon_3)^2 + (\varepsilon_3 - \varepsilon_1)^2}{2}\right]^{\frac{1}{2}} \quad (2\text{-}6)$$

2.3.5.3 Brittle Coulomb-Mohr Stress Failure Theory

The Brittle Coulomb-Mohr (BCM) stress-based failure theory can be used to predict failure for materials whose strengths in tension (σ_{yt}) and compression (σ_{yc}) are not equal. BCM has three conditional cases based on the principal stresses and whether the element is undergoing pure tension, pure compression, or shear. The safety factor using BCM is found using [123]

$$n = \frac{\sigma_{yt}}{\sigma_1} \qquad \sigma_1 \geq \sigma_3 \geq 0 \quad (2\text{-}7a)$$

$$n = \left(\frac{\sigma_1}{\sigma_{yt}} - \frac{\sigma_3}{\sigma_{yc}}\right)^{-1} \qquad \sigma_1 \geq 0 \geq \sigma_3 \quad (2\text{-}7b)$$

$$n = -\frac{\sigma_{yc}}{\sigma_3} \qquad 0 \geq \sigma_1 \geq \sigma_3 \quad (2\text{-}7c)$$

2.3.5.4 Brittle Coulomb-Mohr Strain Failure Theory

The Brittle Coulomb-Mohr (BCM) strain-based criteria follows the same theory as the stress analog and is used to predict failure using the yield strains in tension (ε_{yt}) and compression (ε_{yc}). The BCM strain equivalent has three conditional cases based on the principal strains and whether the element is undergoing pure tension, pure compression, or shear. The safety factor using BCM is found using

$$n = \frac{\varepsilon_{yt}}{\varepsilon_1} \qquad \varepsilon_1 \geq \varepsilon_3 \geq 0 \quad (2\text{-}8a)$$

$$n = \left(\frac{\varepsilon_1}{\varepsilon_{yt}} - \frac{\varepsilon_3}{\varepsilon_{yc}}\right)^{-1} \qquad \varepsilon_1 \geq 0 \geq \varepsilon_3 \quad (2\text{-}8b)$$

$$n = -\frac{\varepsilon_{yc}}{\varepsilon_3} \qquad 0 \geq \varepsilon_1 \geq \varepsilon_3 \quad (2\text{-}8c)$$

2.3.5.5 Normal Principal Stress Failure Theory

The normal principal stress failure theory assumes that material failure occurs when the principal stresses on an element exceed the tensile or compressive yield stresses. The criterion considers the lowest non-negative safety factor using two cases [82]. The safety factor using the principal stress theory is found using

$$n = \frac{\sigma_{yt}}{\sigma_1} \tag{2-9a}$$

$$n = -\frac{\sigma_{yc}}{\sigma_3} \tag{2-9b}$$

2.3.5.6 Normal Principal Strain Failure Theory

The normal principal strain failure criteria follows the same theory as the stress-based analog. The theory characterizes material failure to occur when the principal strains on an element exceed the tensile or compressive yield strains. The safety factor using the principal strain theory is found using

$$n = \frac{\varepsilon_{yt}}{\varepsilon_1} \tag{2-10a}$$

$$n = -\frac{\varepsilon_{yc}}{\varepsilon_3} \tag{2-10b}$$

2.3.5.7 Hoffman Stress Failure Theory

The Hoffman stress failure theory was developed for brittle materials and accounts for differing tensile and compressive strengths. Unlike the von Mises stress failure criterion, Hoffman stress theory considers both the deviatoric and hydrostatic stress components as shown in Figure 2-11 [124].

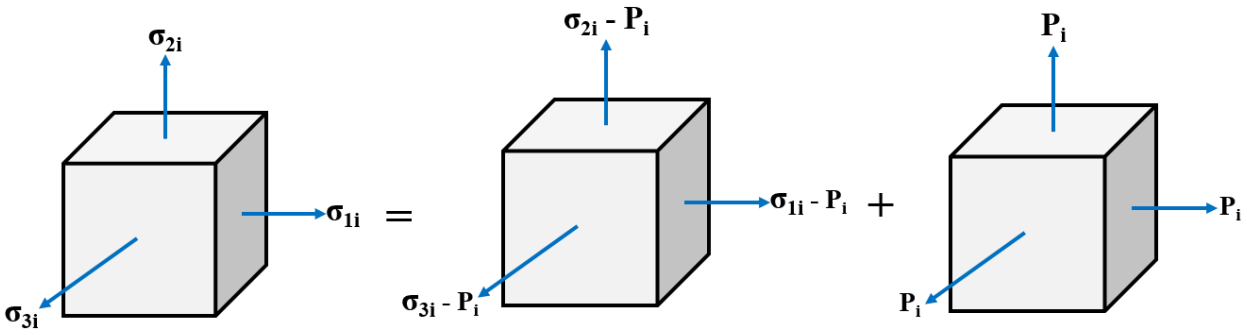

Figure 2-11. The stress field on an element can be decomposed into deviatoric and hydrostatic components. The deviatoric component consists of the unequal principal stresses (σ) and results in element distortion (change in angle or aspect ratio). For the hydrostatic component, the element is subjected to the same normal stress, P_i, causing a constant volume change.

The Hoffman stress criterion assumes that element failure is due to the formation and propagation of cracks in tension and shear. The compressive hydrostatic component increases element strength by closing material cracks, while the deviatoric component always contributes to failure. Unlike other failure criteria, a safety factor greater than or equal to 1 is considered failure, and anything less than 1 is safe. The Hoffman stress safety factory can be calculated using the following equation [103]

$$n = \left(\frac{1}{2\sigma_{yt}\sigma_{yc}}\right)[(\sigma_1-\sigma_2)^2 + (\sigma_1-\sigma_3)^2 + (\sigma_2-\sigma_3)^2] + \left[\left(\frac{1}{\sigma_{yt}}\right) - \left(\frac{1}{\sigma_{yc}}\right)\right](\sigma_1+\sigma_2+\sigma_3) \qquad (2\text{-}11)$$

2.3.5.8 Hoffman Strain Failure Theory

The Hoffman strain analog follows the same theory as the Hoffman stress, but with the stresses replaced by the principal strains and yield strains [103]. Like the stress-based criterion, Hoffman strain theory assumes failure occurs due to the formation and propagation of cracks in tension and shear. A safety factor greater than or equal to 1 is considered failure, and anything less than 1 is safe. The Hoffman strain safety factor can be calculated using [99,103]

$$n = \left(\frac{1}{2\epsilon_{yt}\epsilon_{yc}}\right)[(\epsilon_1-\epsilon_2)^2 + (\epsilon_1-\epsilon_3)^2 + (\epsilon_2-\epsilon_3)^2] + \left[\left(\frac{1}{\epsilon_{yt}}\right) - \left(\frac{1}{\epsilon_{yc}}\right)\right](\epsilon_1+\epsilon_2+\epsilon_3) \qquad (2\text{-}12)$$

2.4 Bone & Muscle

Bones and skeletal muscle are intrinsically linked through voluntary loads which are applied onto the femur through muscle contractions [26]. An improved understanding of muscle-bone relationships may be beneficial in developing hip fracture prevention strategies (e.g., exercise therapy). Previous studies have shown that muscle area measurements from MRI scans are a surrogate measure of muscle forces at the hip, and are positively associated with aBMD ($p < 0.001$) in elderly adults [125–127]. Conversely, as muscle mass begins to decline with age and is replaced by fat and connective tissue, fat may be a predictor of bone strength in addition to fall risk [59,126]. At present, it is unknown what role muscle and adipose tissue have on hip strength using MRI.

2.4.1 Links Between Bone and Muscle

Morphologically, muscle has been previously related to bone-characterizing strength metrics. Two prior studies with large populations reported significant correlations between muscle cross-sectional area and commonly used bone strength metrics at the proximal shaft. Rupaimoole et al., found significant (p <0.001) correlation coefficients between muscle area and cortical area (0.43 for male, 0.47 for female), cortical thickness (0.34 for male, 0.39 for female), and buckling ratio (-0.14 for male, -0.25 for female) [128]. Similarly, Högler et al., reported a strong correlation between muscle area and cortical area ($r^2 = 0.91$ for male, $r^2 = 0.88$ for female) [129]. Conversely, Niinimäki et al. assessed the relationship between impact loading, cross-sectional bone geometry (cortical area, trabecular area, and torsional rigidity at the intertrochanter and shaft), and gluteus maximus size with conflicting findings. In this study, they found that muscle cross-sectional area was only associated with bone properties at the mid-shaft and suggested that activity (ground impact loading magnitude and frequency) may have a more direct effect on bone strength than muscle loading [130]. However, the study was limited as it did not assess functional muscle groups,

did not evaluate the femoral neck strength, and reported marginal means instead of correlation coefficients. As such, the degree of influence muscle and IntraMat areas have on bone strength is unclear.

Differing from cumulative muscle measurements, one study found that increased IntraMAT may compromise muscle performance and increase susceptibility to fracture in older adults [131]. Highlighting the significance of adipose tissue infiltration, Schafer et al. found that IntraMAT area measurements were positively associated with a 19% increase in incidental clinical fall fractures in elderly adults in a study of 331 participants [132]. These results suggest that IntraMAT may be associated with weak bone strength.

To date, the association between muscle and IntraMat areas with FE outcomes has not been extensively explored. Lang et al. explored how femoral failure load and muscle cross-sectional area adapted due to physical activity interventions (squatting, hip abduction/adduction movements) using pre and post-training QCT images of 22 subjects (aged 25-55) [133]. This research found that physical activity resulted in a 7.4% increase in muscle cross-sectional area, a 9% increase in stance failure load, and no change from baseline for the fall configuration failure load [133]. The study provides support that exercises focused on hip muscles will improve both muscle area and bone strength; however, the association of muscle and bone outcomes was not quantitatively explored as relating to exercise regimes was the primary objective.

An improved understanding of the muscle-bone relationship at the hip using MRI may aid in designing improved preventative hip fracture strategies. It is unknown how muscle area and intramuscular adiposity at the hip are related to MR-FE derived bone strength outcomes. There is a current opportunity to explore relationships between muscle properties and FE-derived bone outcomes.

2.5 Characterizing Muscle Properties

At the upper-thigh, soft tissue is generally separated into muscle, IntraMAT, and cumulative (muscle and IntraMAT) area measures, with prior studies excluding subcutaneous fat, as shown in Figure 2-12 [35,60,133,134]. The upper-thigh region has also been divided into the four muscle groups (hip extensors, adductors, flexors, and knee extensors) distinguished by their movement functionalities. Measures of cumulative area at the hip using MRI have a previously reported *in vivo* precision error ($CV\%_{RMS}$) ranging from 1.3-4.5% [33]. *In vivo* measurement precision of IntraMat area measurements (individual muscle groups and total) though have not been previously reported.

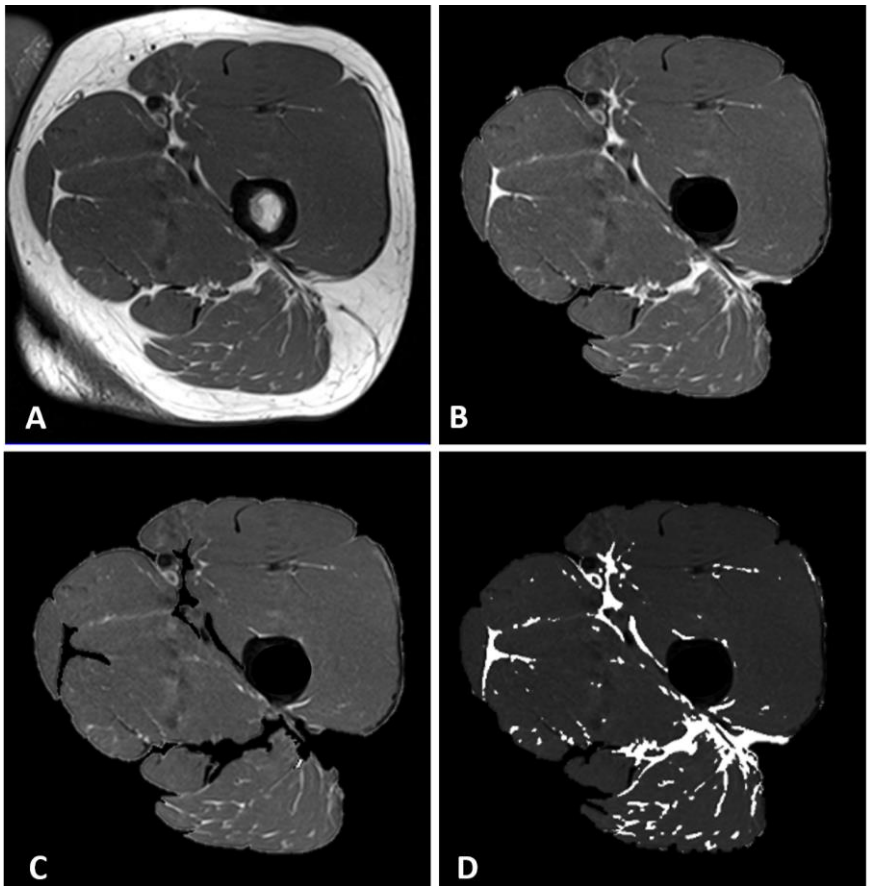

Figure 2-12. A: MRI slice at the hip; B: removal of the subcutaneous fat surrounding the muscle; C: removal of the intermuscular adipose tissue (InterMAT) and subcutaneous adipose tissue; D: muscle with emphasized intramuscular fat (IntraMAT in white).

2.6 Precision

Knowledge of measurement error is important to establish the error of the technique and identify the most precise outcomes and failure criteria which should be used for strength assessment. Glüer et al. established conservative recommendations of 27 DOF to result in an upper 90% confidence limit of +30% of the mean precision error [112]. To calculate the short-term precision of a method, root-mean squared coefficients of variation ($CV\%_{RMS}$) are used and calculated as follows [112]

$$CV\%_{RMS} = \sqrt{\sum_{j=1}^{m} \frac{\left(\frac{SD_j}{\bar{x}_j} \text{x } 100\%\right)^2}{m}} \tag{2-13}$$

And the standard deviation (SD_j) between repeat measurements can be obtained using

$$SD_j = \sqrt{\sum_{i=1}^{n} \frac{\left(x_{ij} - \bar{x}_j\right)^2}{n-1}} \tag{2-14}$$

where m is the number of participants in the study, $\bar{x}_j$ is the mean of the measurements, x_{ij} is the measurement value, and n is the number of repeated scans for each participant. An understanding of the precision error is critical as it identifies parameters which may be best suited for future research related to MR-FE estimates of hip strength.

The International Society of Clinical Densitometry recommends estimating the least significant change to determine if observed skeletal differences are true and greater, with 95% confidence, than the measurement error. LSC is estimated using the root-mean squared coefficient of variation and an adjusting Z-score (2.77) derived from the 95% confidence interval. LSC is specifically defined as 2.77 x $CV\%_{RMS}$ [135]. Essentially, LSC is a quantitative metric to ensure observed differences or changes are sufficiently larger than precision errors of a technique.

2.7 Summary of the literature

1. Hip fractures are a serious life-threatening issue. Fractures typically occur within the femoral neck, intertrochanteric, and shaft regions during sideways fall loading.
2. The proximal femur's strength can only be directly determined using destructive mechanical testing. As such, non-invasive imaging modalities and loading are critical to evaluate bone strength *in vivo.* A greater understanding of hip strength and relationships with muscle properties can also potentially lead to improvements in preventative strategies (e.g., exercise therapy) aimed at reducing hip fragility and risk of fracture.
3. Improved methods for assessing proximal femoral strength beyond aBMD measures are needed to more accurately identify individual's bone strength. By accounting for subject-specific geometry, bone material distribution, and tissue properties, FE modeling provides pertinent strength-describing mechanical outcomes beyond DXA measures.
4. MRI can be used to non-invasively image the hip *in vivo* without ionizing radiation exposure to the radiosensitive pelvis. MRI is a suitable modality for imaging muscle, fat, and bone.
5. MRI combined with FE modeling has been used in previous studies as a method of characterizing bone strength. The *in vivo* precision error of MR-FE mechanical outcomes at the hip for fall and stance loading are currently unknown. Knowledge of measurement error is important to establish the reliability of the technique and identify which outcomes can be used for strength assessment.
6. Muscle and bone are intrinsically linked through habitual loading. Relatedly, muscle and IntraMAT areas are associated with increased risk of fracture following a fall. However, the association of muscle and fat properties with MR-FE bone outcomes is unknown.

CHAPTER 3
RESEARCH QUESTIONS AND OBJECTIVES

3.1 Research Questions

To address the literature gaps, my research questions are:

1. What are the short term, *in vivo* precision errors of MR imaging based FE estimates of bone strength at the proximal femur?
2. Are FE-derived outcomes of the proximal femur associated with surrounding muscle and fat properties?

3.2 Research Objectives

To address my research questions, my thesis objectives were to:

1. Characterize the short-term *in vivo* measurement precision of MR-FE outcomes of the proximal femur for configurations simulating fall and stance loading.
2. Explore associations between upper thigh muscle and fat area with MR-FE failure loads of the proximal femur.

CHAPTER 4

MR-FE MODELING OF THE PROXIMAL FEMUR: AN *IN* VIVO PRECISION STUDY

4.1 Synopsis

Chapter 4 addresses the *in vivo* measurement reproducibility of MR-FE outcomes at the proximal femur for configurations simulating fall and stance loading. The short-term precision errors were ≤ 11.8% for the FE outcomes. Precision of the MR-FE outcomes ranged from 3.3% to 11.8% for stress and strain-based mechanical outcomes, and 6.0% to 8.4% for failure loads. The study provides evidence that MR-FE outcomes are a promising non-invasive technique for monitoring femoral strength *in vivo*.

4.2 Introduction

Hip fractures are a serious life-threatening injury that results in chronic disabling pain, depression, and mortality [2,39]. DXA aBMD measurements are the current clinical standard for assessing femoral strength; however, this technique is insufficient due to its planar imaging and inability to distinguish between cortical and trabecular bone [64]. Subject-specific FE modeling of the hip has been used to non-invasively estimate bone strength *in vivo* and provides a comprehensive assessment of strength by considering 3D geometry, bone material distribution, and tissue properties [61,102,109].

Within the hip, fracture typically occurs at the neck, intertrochanteric, and proximal shaft regions. As such, strength assessment studies and protocols have predominately focused on these three regions [42,114,136]. Previously, *in vivo* FE models of the hip have been developed using MRI, with studies primarily focusing on predicting failure regions and assessing hip strength between different populations [105,114,137]. However, the precision (repeatability) of FE derived mechanical outcomes (stress/strain) and failure loads using MRI are currently unknown.

Knowledge of the measurement error is important to establish the trustworthiness of the technique and to identify which outcomes and failure criteria should be used to assess hip strength.

The objective of the study was to characterize the short-term *in vivo* measurement precision of MR-FE outcomes of the proximal femur for configurations simulating fall and stance loading.

4.3 Methods

4.3.1 Study Sample

Thirteen healthy participants (5 males and 8 females) with ages ranging from 21 to 68 years (mean age: 30.6, standard deviation (SD): 12.5 years), and weights ranging from 54 to 105 kg (mean: 72.1, SD: 15 kg) were recruited as part of a previous study at the University of Saskatchewan [33]. Study approval was obtained from the University of Saskatchewan Biomedical Research Ethics Board and informed consent was provided by all participants.

4.3.2 MRI Scan Parameters

MRI scans of the left proximal femur were obtained from a previous research study (2014) [33]. Axial images (relative to the orientation of the participant) of the hip were obtained using a clinical 1.5T scanner (MAGNETOM Avanto, Siemens, Germany) with a 6-channel body array coil positioned over the hip region. Each participant was positioned supine with their left leg extended and externally rotated 15˚. Scanned image volumes included ~2 cm superior to the femoral head and concluded ~5 cm inferior to the lesser trochanter. A T1-weighted turbo spin echo sequence was used with the following parameters: TR 616 ms, TE 12 ms, 2 excitations, 180˚ flip angle, 0.45x0.45 mm in plan pixel size, 4 mm slice thickness, ~4.5 minute scan time, ~ 40 images. Each participant was scanned three times with a repositioning involving a short walk occurring between repeat scans.

4.3.3 Image Homogeneity Correction

Intensity shading inhomogeneity, commonly known as “bias field”, was present in the original MRI scans, likely due to non-uniformity in the radio-frequency (RF) hip coil [138]. 3D Slicer, an open-source software platform for medical imaging was used in conjunction with a non-parametric, non-uniform intensity normalization module (N4ITK) to interactively correct the image inhomogeneity [96,139,140]. Each original scan of the proximal femur was individually loaded and processed using the correction module. Each image was then visually checked for shading improvement as shown in Figure 4-1.

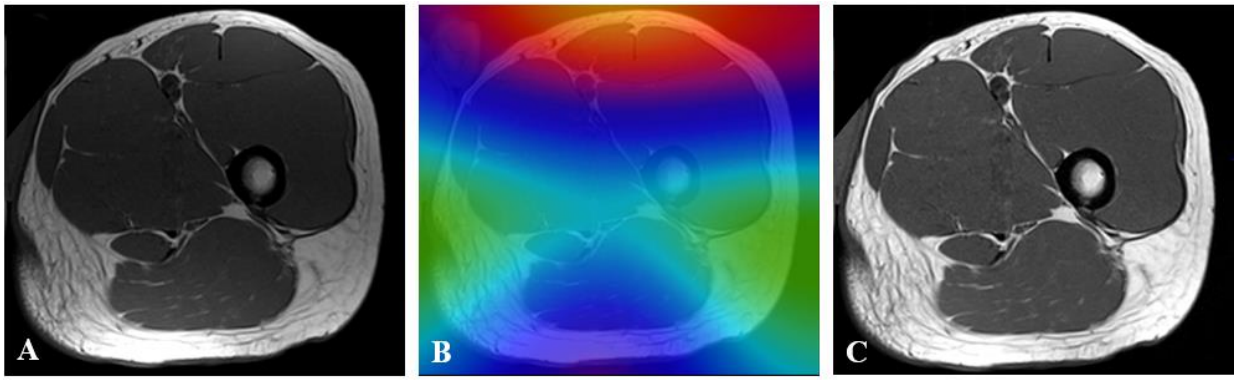

Figure 4-1. Uncorrected MR image slice with visible intensity shading inhomogeneity (A); the calculated bias field mask overlaid onto the uncorrected image slice (B); corrected image slice (C)

4.3.4 Segmentation and Interpolation

Using commercial software (Analyze 12.0: Mayo Foundation, Rochester, MN, USA), adjusted MRI scans were semi-automatically segmented (i.e., outlined) to delineate the proximal femur from surrounding soft tissue. Each image slice was segmented in the transverse plane followed by manual correction via a stylus and touchscreen tablet (Cintiq 21uX, Wacom, Krefeld, Germany). Subject-specific thresholds were used to define the cortical bone surface and separate it from the soft tissue. To determine the thresholds, we used the half-maximum height (HMH) method for optimizing boundary delineations and minimizing manual corrections between participant scans

[141,142]. The HMH method defines the optimal threshold value of the cortical-soft tissue boundary as the midpoint between the maximum and minimum intensity values along a row of pixels crossing the boundary. The thresholds were defined at a site approximately 2 cm below the lesser trochanter on the femoral shaft. All segmentations were performed by a single researcher (KM) and generated a binary mask.

To start the semi-automatic segmentation, a region-growing seed was placed in the cortical bone region of the image slice. The periosteal boundary of the cortical bone was then grown until the HMH threshold value was reached. Using the stylus and touchscreen tablet, the region boundary was manually corrected to ensure the entire proximal femur was correctly included within the segmented image (Figure 4-2). The 2D segmentations of each slice were then combined to form an anisotropic discrete 3D object map of the proximal femur.

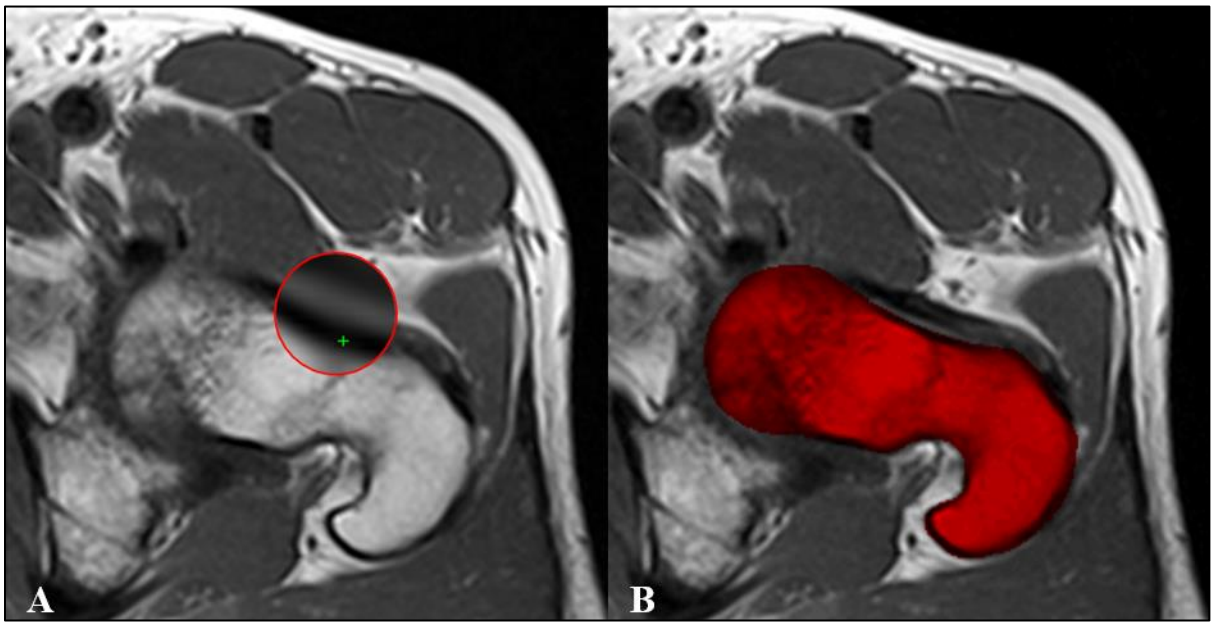

Figure 4-2. Illustration of the semi-automatic segmentation of a 2D image slice at the greater trochanteric region. Seed placement (green "+" within the magnified region) within the cortical bone (A); Defined proximal femur overlay using the HMH threshold (B).

The original discrete MRI scans and segmentations were cubic interpolated to create isotropic cubic arrays (from 0.45 x 0.45 x 4 mm to 0.45 x 0.45 x 0.45 mm). Commercial software (Analyze 12.0) was used for the interpolation. By applying interpolation, the jagged, stair-step geometry of the original scans was corrected, providing a more anatomically correct structure.

Following interpolation, binary masks were adjusted in the coronal plane to more accurately define bone geometry. With improved binary masks, the secondary segmentation in the alternative plane helped reduce delineation precision errors by minimizing the effect of the participants being repositioned between scans. The same subject-specific HMH thresholds were used for the transverse and coronal segmentations.

4.3.5 Alignment

To remove variability occurring due to subject repositioning between repeat participant scans, image volumes (original scans and masks) were realigned into a common orientation using custom coding (Matlab 2018a; MathWorks, Natick, MA, USA). From the common position, we then aligned the images into the frequently studied fall and stance orientations [45,82,105,143]. First, we identified the femur long axis and the femoral head center point of the MRI scans (Figure 4-3). Next, we established temporary orthogonal x, y, and z axes where the long axis of the bone was vertical and planar with the center of the femoral head. Thirdly, we rotated the body about the center of the femoral head 45 degrees in the coronal plane to temporarily remove the greater trochanter and identify the neck axis. Fourthly, we rotated the volume about the z-axis such that the neck axis was aligned with the x-z plane (coronal plane) and the femur long axis was vertical, providing the common orientation. Finally, we rotated the images from the common orientation to the stance and fall loading configurations:

- Stance configuration: Shaft long axis rotated 20° from the vertical [45,143]

- Fall configuration: Neck axis rotated at 15° of internal rotation and the shaft long axis 10° of adduction in reference to the ground [49,50,82,105,144]

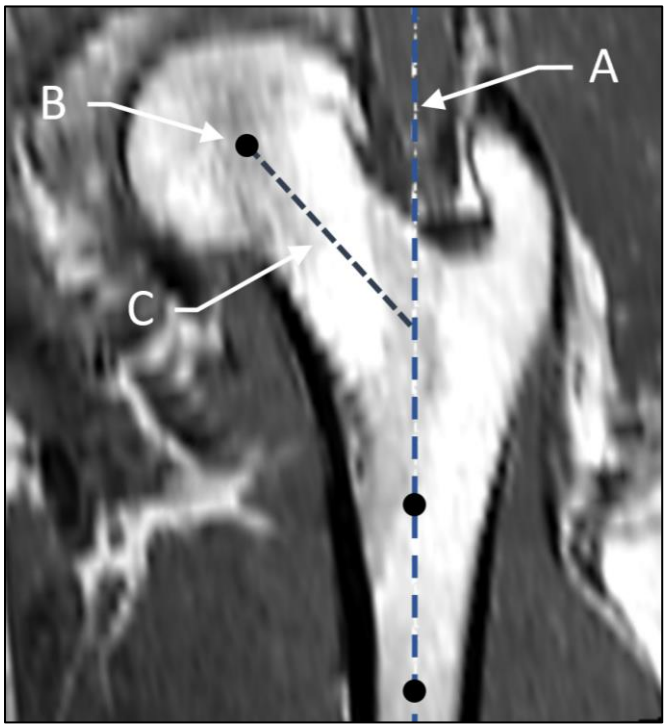

Figure 4-3. MRI scans were aligned into a common orientation (shown) and then rotated into fall and stance configurations prior to FE model generation. The long axis of the femur was found by determining the centroid of the proximal and distal shaft sites, with two points defining the vertical axis (A). The center point of the femoral head was found by fitting a sphere to the circular region (B). The image was then rotated 45° in the coronal plane using a temporary axis to remove the distal shaft and greater trochanter and orient the neck vertically. We then defined the neck vector as the vertical line passing through the femoral head center and intersecting with the long axis of the femur (C).

4.3.6 FE Modeling

FE models representative of stance and sideways fall loading configurations were generated from the realigned MRI volumes and segmentations. To identify an appropriate element size, we performed a preliminary mesh convergence study. Using custom algorithms (Matlab), we converted each voxel into an 8-noded hexahedral element with dimensions corresponding to the 0.45 mm voxel size. Bone material properties were assumed to be linearly elastic and isotropic,

with the elastic moduli of each voxel computed from the image intensity. Voxel-specific BVF's were computed from the image intensity via BVF = 1 – (Int_{voxel} / Int_{max}) [11]. We used a custom MRI phantom to verify that a linear relationship exists between image intensity and BVF (R^2 = 0.9995) (Appendix A). We related BVF to apparent density, and then ash density to apparent density using previously published relations (Table 2-5) [85,120]. Using the cortical bone elastic modulus equation proposed by Öhman et al. for the proximal femur [119], and substituting in the density relations, the final equation we used to calculate the elastic modulus from the intensity of each voxel was:

$$E = 12.9\left[1.08\left(1 - \frac{Int_{voxel}}{Int_{max}}\right)\right]^2 \quad (4\text{-}2)$$

where E is the elastic modulus in MPa, Int_{voxel} is the intensity of each voxel, and Int_{max} is the maximum fat intensity in the scan. A Poisson's ratio of 0.3 was assumed for all elements [145].

Nodal connectivity and material properties of the proximal femur were imported into ABAQUS software (version 6.13, Providence, RI, USA) for loading and analysis. For the stance loading configuration (Figure 4-4), we applied an initial distributed load over the femoral head. The distal shaft was fully constrained as in previous studies [45,103,108]. For the sideways fall configuration (Figure 4-4), we applied a distributed load over the femoral head. A hinge-type boundary condition was applied on the distal shaft of the fall models, allowing nodes to freely rotate within the frontal plane and all other DOF's constrained. The most lateral nodes of the greater trochanter were fully constrained in the direction of the force [38,105,108,146]. Force magnitude was arbitrary for the models as the linearity allowed for the results to be scaled for any magnitude.

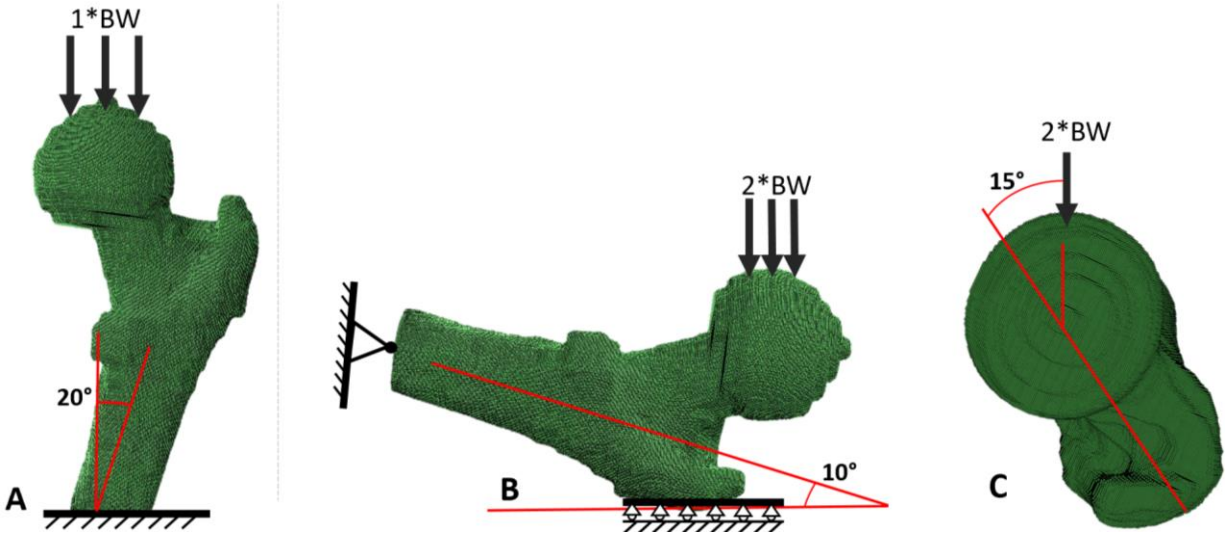

Figure 4-4. Stance and fall loading configurations of the FE models. The shaft long axis was rotated 20° from the vertical and an initial distributed load applied over the femoral head for the stance models (A). For the fall configuration, the femoral shaft was tilted 10° with respect to the ground (B) and the neck axis was internally rotated 15° (C). The distal shaft was constrained with a hinge-type boundary condition (prohibiting displacements but allowing rotations), and the greater trochanter nodes were restrained in the direction of the distributed load.

Strain and equivalent stress limits were used for cortical and trabecular bone. We assigned a tensile strain limit of 7000 μstrain for the proximal femur [122,147]. The equivalent tensile stress limit was assigned by multiplying the tensile strain limit by the respective element's elastic modulus [99]. As bone is stronger in compression than tension, the tensile and compressive strain limits ($\varepsilon_{yt}, \varepsilon_{yc}$) and stress ($\sigma_{yt}, \sigma_{yc}$) limits were related using the ratios $\varepsilon_{yt}/\varepsilon_{yc}$ and σ_{yt}/σ_{yc}, andare equal to 0.7 [48,103]. A ratio of 0.7 was selected as Keyak et al., evaluated the performance of various failure criteria and ratios for femoral FE models and found tensile-to-compressive ratios less than 0.7 to be poor predictors of failure load [103].

Each model was solved in ~3.5 hours using commercial FE software ABAQUS. For each model, the von Mises stress, principal stresses, and principal strains at the centroid of each element were calculated and outputted by ABAQUS.

4.3.7 Additional FE Outcomes

FE-derived stress/strain, failure loads from eight different failure theories were calculated (equations 2-4 to 2-13 using custom Matlab coding). The applied force was linearly scaled to determine the failure load [kN] which would cause 5% of the elements (approximately 150 mm^3 volume) to fail according to the von Mises stress/strain yield, BCM stress/strain, normal principal stress/strain, and Hoffman stress/strain criteria [99,103,104,124]. For the failure criteria, a safety factor of less than 1 indicated element failure for all the theories except the Hoffman stress/strain, whereby failure occurred when the safety factor was greater than or equal to 1 [99,103].

4.3.8 Regional Analysis

The FE outcomes were analyzed at 4.5 mm thick anatomical regions of interest (Figure 4-5) at the neck, intertrochanteric, and shaft. The regions were selected based on common critical failure regions and automatically defined using anatomical landmarks and custom coding (Matlab) [38,46]. The regions were defined at:

- Neck: Center of the femoral neck axis between the head center and vertical shaft axis
- Intertrochanteric: The bi-sector of the angle between the neck and shaft
- Shaft: 20 mm below the inferior edge of the lesser trochanter

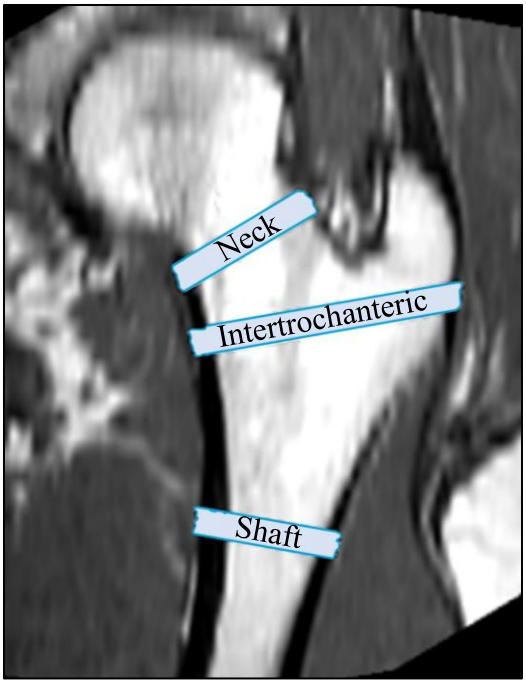

Figure 4-5. FE outcomes were reported at 4.5 mm thick regions at the femoral neck, intertrochanteric, and shaft. Regions were automatically defined using anatomical landmarks.

For each orientation and region, the mean von Mises stress, von Mises strain, principal stresses, and principal strains were calculated. To quantify bone strength, we calculated the failure loads to cause 5% of the elements to fail within each of the 3 regions of interest.

4.3.9 Statistical Analysis

We assessed the short-term *in vivo* precision error of each outcome via $CV\%_{RMS}$ [112]. With 13 participants scanned 3 times, this provided 26 degrees-of-freedom (DOF = # participants * (# scans - 1)), which met recommendations by Glüer et al [112]. With this DOF, we established a precision error with an upper 90% confidence limit less than 31% (e.g., if the precision error is 5%, the upper 90% confidence limit is less than 6.6%) [112]. We report mean values for each outcome for numerical comparisons. Short-term precision was also assessed in absolute terms using the root mean square standard deviation (SD_{RMS}) of the 3 repeat measures.

4.4 Results

For the fall configuration, $CV\%_{RMS}$ precision errors of the stress/strain measures averaged 7.9% and ranged from 5.3% to 11.7% (Table 4-1). For the stance configuration, $CV\%_{RMS}$ precision errors of the stress/strain measures averaged 7.8% and ranged from 3.3% to 11.8%. $CV\%_{RMS}$ for the strain measures ranged from 7.0% to 11.8%, and 3.3% to 7.9% for the stress measures. Stress/strain precision errors appeared similar between the femoral neck, intertrochanteric, and shaft regions.

$CV\%_{RMS}$ precision errors for failure loads in the fall configuration averaged 7.7% and ranged from 6.0% to 9.5% (Table 4-2). $CV\%_{RMS}$ precision errors of failure loads for the stance configuration averaged 7.5% and ranged from 6.3% to 8.2%. Mean failure load precision errors were < 7.6% at the femoral neck, < 7.5% at intertrochanteric region, and < 7.7% at the shaft.

Table 4-1. Precision results for the MR-FE mechanical outcomes for the fall and stance loading configuration (13 participants, 3 scans each, 26 degrees of freedom). Mean values are presented at three critical regions (4.5 mm thick) as defined using anatomical landmarks. Precision is reported using root mean square standard deviations (SD_{RMS}) and coefficients of variation ($CV\%_{RMS}$)

Orientation	Outcome	Neck					Intertrochanteric					Shaft				
		Mean	*Max*	*Min*	SD_{RMS}	$CV\%_{RMS}$	*Mean*	*Max*	*Min*	SD_{RMS}	$CV\%_{RMS}$	*Mean*	*Max*	*Min*	SD_{RMS}	$CV\%_{RMS}$
Fall	von Mises stress [MPa]	4.7	6.9	3.3	0.3	5.4	2.8	4.2	1.8	0.1	5.3	3.4	5.1	1.6	0.2	5.5
	von Mises strain [μstrain]	1021.1	2547.2	465.0	140.7	9.0	2151.6	7540.9	404.3	424.1	11.5	513.2	851.3	165.7	60.3	11.7
	Max. principal stress [MPa]	1.9	2.9	1.1	0.1	6.2	1.9	2.2	0.8	0.1	6.2	1.4	3.3	0.8	0.1	6.2
	Min. principal stress [MPa]	-3.2	-2.4	-5.2	0.2	6.1	-1.7	-1.0	-2.6	0.1	6.4	-1.7	-0.8	-3.2	0.1	6.7
	Max. principal strain [μstrain]	645.6	1466.9	298.5	81.2	9.6	1249.2	4239.4	258.8	159.7	8.8	412.9	649.7	132.4	41.8	9.5
	Min. principal strain [μstrain]	-995.7	-460.9	-2729.6	152.4	9.4	-2258.6	-408.4	-7903.6	259.1	9.0	-399.0	-133.6	-655.1	35.0	9.1
Stance	von Mises stress [MPa]	1.5	2.5	0.9	0.1	7.2	0.7	1.1	0.5	0.0	4.8	1.8	3.0	1.1	0.1	6.0
	von Mises strain [μstrain]	250.4	354.4	144.3	26.2	9.9	224.7	606.3	89.9	43.3	11.4	253.4	392.3	168.9	36.2	11.8
	Max. principal stress [MPa]	0.3	0.6	0.1	0.0	7.2	0.3	0.3	0.1	0.0	7.2	0.2	0.8	0.2	0.0	6.9
	Min. principal stress [MPa]	-1.2	-0.8	-2.0	0.1	7.9	-0.6	-0.4	-1.0	0.0	6.9	-1.4	-1.0	-2.0	0.1	3.3
	Max. principal strain [μstrain]	158.3	245.7	92.1	14.8	9.0	201.4	620.4	60.3	26.2	8.7	149.2	240.4	88.9	9.4	7.0
	Min. principal strain [μstrain]	-255.2	-138.6	-380.8	23.6	9.3	-189.2	-87.6	-390.0	14.0	8.7	-234.5	-166.1	-316.4	18.5	7.7

Table 4-2. Precision results for the MR-FE failure loads for the fall and stance loading configuration (13 participants, 3 scans each, 26 degrees of freedom). The mean failure loads [kN] to cause 5% of the elements to fail at three critical regions (4.5 mm thick) are presented. Precision of each failure criteria is reported using root mean square standard deviations (SD_{RMS}) and coefficients of variation ($CV\%_{RMS}$)

	Outcome	Neck				Intertrochanteric				Shaft			
		Mean	*Range [kN]*	SD_{RMS}	$CV\%_{RMS}$	*Mean*	*Range [kN]*	SD_{RMS}	$CV\%_{RMS}$	*Mean*	*Range [kN]*	SD_{RMS}	$CV\%_{RMS}$
Fall	BCM stress	9.2	15.8-5.1	0.7	7.0	12.1	21.4-4.8	0.9	7.1	14.9	26.4-8.6	1.2	7.5
	BCM strain	8.7	15.9-4.1	0.7	8.2	12.0	23.4-5.8	0.9	7.3	13.8	24.8-6.1	1.0	7.8
	Normal principal stress	7.7	13.6-3.9	0.6	8.1	9.8	13.6-4.7	0.9	8.5	16.0	20.9-6.9	1.1	7.5
	Normal principal strain	7.5	10.9-2.8	0.5	6.5	9.5	18.6-2.4	0.6	6.0	16.4	20.1-5.4	1.4	8.3
	von Mises stress	8.4	13.2-4.5	0.6	8.1	11.0	20.0-4.5	0.8	8.2	14.9	20.6-8.6	1.3	8.4
	von Mises strain	8.2	15.2-4.0	0.8	8.3	10.3	19.3-6.2	1.0	9.0	14.3	20.2-8.9	1.0	9.5
	Hoffman stress	9.5	13.8-5.4	0.7	7.0	12.4	20.1-5.5	0.8	6.6	15.3	18.6-9.0	1.0	6.4
	Hoffman strain	8.3	13.7-2.8	0.7	7.4	10.8	19.1-2.8	0.9	7.7	13.6	18.3-8.2	1.2	8.2
Stance	BCM stress	14.5	19.9-10.2	1.1	7.0	12.6	20.2-6.4	1.0	7.6	14.5	23.7-10.5	1.1	7.5
	BCM strain	13.9	19.5-10.1	1.1	8.1	11.9	20.4-5.3	0.9	7.6	14.1	24.9-8.7	1.0	7.7
	Normal principal stress	10.8	17.4-6.8	0.9	8.0	13.8	18.9-7.3	13.8	8.0	11.9	18.0-6.7	0.9	7.1
	Normal principal strain	10.9	14.6-6.1	0.9	7.9	13.6	19.5-5.4	1.0	6.9	12.1	20.6-8.4	0.9	7.4
	von Mises stress	11.1	15.7-7.9	0.9	8.0	11.4	14.3-6.7	0.8	7.1	13.4	20.5-9.1	0.9	6.3
	von Mises strain	10.7	13.7-6.7	0.9	8.2	11.5	15.3-6.1	0.8	7.4	13.7	21.0-8.9	1.0	7.2
	Hoffman stress	14.9	18.7-8.1	1.1	6.8	14.5	19.9-6.9	1.1	6.9	15.9	20.1-8.1	1.2	7.8
	Hoffman strain	14.3	18.6-8.1	0.9	6.6	14.6	20.8-7.6	1.1	8.0	14.2	19.6-8.6	1.1	8.1

4.5 Discussion

This study characterized the short-term *in vivo* precision error of MR-FE outcomes of the proximal femur for two loading configurations and three critical regions. To our knowledge, this is the first study to report FE precision errors at the neck, intertrochanteric, and shaft regions using MRI scans. This study complements existing studies which focused on evaluating differences in MR-FE outcomes between groups and provides indication of measurement error [82,105]. Outcomes were reported as mean values (von Mises stress/strain, principal stress/strain) at three critical regions. Additionally, precision errors of estimated failure loads to cause 5% of the elements to fail within a ROI were determined using eight theories (von Mises stress/strain yield, BCM stress/strain, normal principal stress/strain, Hoffman stress/strain).

Generally, the von Mises stress, principal stresses, principal strains, and failure loads had similar and low precision errors (average $CV\%_{RMS}$ <7.5%) except for the von Mises strain criteria which were higher (average $CV\%_{RMS}$ <11%). The high measurement error of the von Mises strain outcomes can be attributed to the small strain values, whereby a small variation resulted in a large precision error. Generally, we consider our small precision errors to be likely attributed to the use of subject-specific thresholds, semi-automatic segmentations, automatic image realignment, and consistent manual user correction.

Our small precision error results are similar, though slightly higher than previous CT-FE findings at the knee which had an average $CV\%_{RMS}$ of < 6% [148]. Similarly, MR-FE precision errors for the fall and stance configurations were comparable with no substantial differences. In comparison to the MR precision study by Johnston et al. which reported precision errors < 7.1% [33], our measurement errors are larger on average. However, our study considered FE outcomes at 3D ROI's whereas Johnston et al. reported metrics based on a single image slice.

To sufficiently recommend a best-suited failure criterion for future MR-FE studies, various parameters including precision error ($CV\%_{RMS}$), explained variance (R^2), and ability to capture changes or differences are needed for consideration. With regards to precision errors, the five failure theories assessed in this study were similar and provided low measurement error with average $CV\%_{RMS}$ <7.6%. Though, a large range of estimated failure loads may indicate a more sensitive criteria for identifying differences in bone strength for MR-FE. In this case, BCM stress generally had the largest failure load range for the loading orientations. In line with this finding, and the relatively low precision error, BCM stress may best characterize hip strength of the theories considered. Further research is needed to evaluate experimentally derived failure loads against MR-FE derived estimates acquired via BCM stress.

The precision results of the study may guide future longitudinal and comparative studies in characterizing strength. The least significant change (LSC) (recommended by the International Society of Clinical Densitometry) is used to determine if observed skeletal differences are true and greater, with 95% confidence, than the measurement error. LSC is specifically defined as 2.77 x $CV\%_{RMS}$ (two-tailed with 95% confidence) [135]. In the MR-FE study by Abe et al., they found that fracture loads acquired via the principal strain criterion were 14-26% greater ($p < 0.05$) for high-impact competitive athletes (Triple jump, high jump, and endurance runners) compared to habitually active controls [82]. Using our precision results, the LSC of our failure theories range from 16.6-26.3%, which is less than the previously observed difference [82]. To further emphasize the potential of our LSC results, Hanieh et al. found differences that the minimum principal stress was, on average, 75% higher in non-healthy knees versus normal knees [148]. Although these results are not for the proximal femur, it provides evidence that bone strength differences can significantly vary amongst healthy and non-healthy participants and is an area of future potential

research for hip studies. These results highlight the potential of MRI to monitor or detect strength differences as MR-FE outcomes appear to offer differences and changes larger than the measurement error.

Numerical results from this study are similar to those published in previous studies, providing a measure of validity to FE outcomes. The mean *in vivo* von Mises stress at the neck for the 13 participants was within the same range (mean: 4.7 MPa, SD: 0.3) as the study published by Abe et al. [105]. Additionally, principal strains of the proximal femur at select locations have been experimentally measured for stance (absolute peak strains ≤ 1102 μstrain) and fall (absolute peak strains ≤ 1284 μstrain) loading configurations by Zani et al, and are similar to those reported in this study at the neck and shaft [48]. The estimated failure loads from our study ranged from 2.4 kN to 23.4 kN and 5.3 kN to 20.8 kN for the fall and stance configurations at the neck and intertrochanteric sites. Previous experimental studies have predominately focused on elderly adult (>70 years of age) cadaveric femurs, with approximate failure loads of 5.2 kN and 8.5 kN for fall and stance loading orientations [38,49,50,61]. Although our reported fracture loads are up to ~2.8 times larger (20.8 kN /8.5 kN) than previous *ex vivo* studies, they are within a reasonable range as Courtney et al., found that young adult (mean age: 31.7, SD: 12.5) femurs are approximately twice as strong as elderly adults (mean age: 73.8, SD: 7.1) [50]. Our study focused on a relatively unstudied young adult population; as such, the failure loads would be larger than elderly adult cadavers.

This research has strengths which require consideration. First, with MR-FE, each voxel of the proximal femur was modeled as a hexahedral element, allowing us to directly map elastic moduli to individual elements. Conversely, when using tetrahedral elements, this requires intensive surface smoothing and careful strategies to map elastic moduli to elements. The surface

smoothing process inherently incorporates voxels outside the original image mask, which can lead to an error during the mapping process. Secondly, we applied a custom algorithm based on anatomic features which automatically aligned MR scans into the fall and stance loading configurations. The automatic re-alignment reduced variation between repeat scans, leading to a lower precision error. Third, we report precision errors at three clinically relevant regions [42,149] for the two commonly studied loading configurations used in literature. The inclusion of different regions and loading configurations provides information of regional properties. Fourth, we have nearly met the conservative sample size (13 participants, 39 scans, 26 DOF) to properly establish the mean precision errors with an upper 90% confidence interval limit less than 30%, as proposed by Glüer et al. [112]. Although our study did not exactly meet the DOF recommendations (28 DOF), the upper 90% confidence limit with our DOF (31%) is comparable to recommendations (30%). These precision results may guide future MR studies in discerning between measurement error and true differences.

This research has limitations which also require consideration. Firstly, due to the large slice thickness (4mm), the true 3D geometry of the femur was difficult to capture and resulted in a jagged structure. The large slice thickness may have resulted in the under/over estimation of bone strength as critical bone features may not have been fully captured in the original MRI scans. To more accurately characterize the shape of the proximal femur, our original scans consisting of 37 slices which were interpolated to 329 slices. This approach led to a more correct shape, but small variations in material properties were not captured. Relatedly, the element size (0.45 mm) used in this study is larger than select 3-T MR-FE studies of the hip (0.234 mm) [10,114]. It would be beneficial to repeat this study with a stronger magnet (3T and above) to better capture variations in shape and material properties. Second, due to the poor signal-to-noise ratios on some scans, it

was difficult to identify the periosteal surface within the greater trochanteric region. To address this, we applied a bias field correction to reduce image inhomogeneity [96,139,140], then defined the boundary using semi-automatic region growing and subject-specific thresholds (HMH) [141], followed by manual segmentation where needed. Operator judgment though had a large effect on femoral segmentations and may have induced error into the analysis. Third, presented MR-FE models of the proximal femur were not validated against mechanical testing, unlike previous QCT-FE studies [103,108]. To address this, we adopted similar boundary and loading conditions as previous studies and compared our numerical results [82,102,104,105,107,108]. However, it would be beneficial to validate MR-FE derived estimates of bone failure load, along with corresponding failure criteria, reported here. Fourth, our study assessed the short-term precision error of relatively young adults (mean age: 30.6, SD: 12.5 years), making it difficult to generalize our results beyond the studied age group. Still, our study provides insight into MR-FE measurement precision and supports the application of MRI for monitoring bone strength differences. A complimentary precision study with older adults is needed for comparison.

4.6 Conclusion

This is the first study to report *in vivo* precision errors for MR-FE outcomes of the proximal femur. Precision errors were less than 12% for the two loading configurations. Precision errors ranged from 3.3% to 11.8% for stress and strain outcomes, and 6.0% to 9.5% for failure loads. Results from this study demonstrate that MR-FE outcomes are a promising non-invasive technique for monitoring femoral strength *in vivo* and may guide future studies in their assessment of femoral strength.

CHAPTER 5
ASSOCIATION OF HIP MUSCLE AND FAT PROPERTIES WITH MR-FE DERIVED FAILURE LOADS OF THE PROXIMAL FEMUR

5.1 Synopsis

Chapter 5 assesses the relationship of muscle and fat properties with MR-FE failure load. The study considered lean muscle and IntraMAT area measurements at the upper thigh and MR-FE derived failure load of the proximal femur for two loading configurations and three ROI's. The study provides evidence that muscle area is strongly associated with MR-FE derived failure loads and may provide valuable information pertaining to characterizing fracture risk as well as mitigation strategies aiming to minimize fracture risk.

5.2 Introduction

Hip fractures are a serious life-threatening injury with the femoral neck, intertrochanteric, and shaft regions being most susceptible to failure [53,149]. To assess femoral strength at critical fracture prone regions, safe, non-invasive, subject-specific *in vivo* MR-FE has been used in the past [43,64,105].

The muscles spanning the hip are linked to femoral bone strength through loads which are applied onto the femur through muscle contractions [26]. Cross-sectional soft tissue area measurements at the upper thigh are a surrogate measure of muscle force [125,126], and may be useful in characterizing bone strength [129]. An understanding of how muscle is related to FE outcomes, most notably failure load, may provide insight and direction into prevention strategies aimed at reducing the risk of fracture.

The objective of this study was to explore associations between upper thigh muscle and fat area with MR-FE failure loads of the proximal femur.

5.3 Methods

5.3.1 Study Sample

Forty-four healthy participants (21 males and 23 females) with ages ranging from 25 to 33 years (mean age: 30.0, SD: 2.1 years), and weight ranging from 54 to 123 kg (mean: 83.9, SD: 16) were previously recruited as part of the Saskatchewan Pediatric Bone Mineral Accrual Study (PBMAS) [150]. Patient descriptions are found in Table 5-1.

Table 5-1. PBMAS participant characteristics

Characteristic	Mean	SD	Range
Age (years)	29.6	2.1	25-33
Weight (kg)	83.9	16.4	54-123
Height (cm)	173.3	9.2	154-189
BMI (kg/m^2)	28.0	5.9	20-52

5.3.2 Image Analysis and FE Modeling

The MRI scan parameters of the left proximal femur are the same as per Chapter 4, and were acquired as part of a previous research study. [150]. The image analysis methodology used for this study has been previously described in detail (Chapter 4). We followed the same process for the bias field correction, segmentation, interpolation, and alignment of the MRI scans.

The regional analysis and load scaling methodology was the same as previously described in detail (Chapter 4). For this analysis, FE outcomes were limited to failure load using the von Mises stress criteria (load to cause 5% of the elements to fail within a region). To derive failure load, we assigned a tensile strain limit of 7000 μstrain, with the equivalent tensile stress limit equal to the strain limit multiplied by the respective element's elastic modulus [99]. Each model was solved in ~3.5 hours using commercial FE software ABAQUS.

5.3.3 Muscle Analysis

Upper thigh MR scans were previously segmented using commercial software (Analyze 10.0: Mayo Foundation, Rochester, MN, USA), delineating the hip extensors, hip adductors, hip flexors, knee extensors, cortical bone, and marrow cavity ~2 cm (40 slices) below the lesser trochanter. The region of interest was selected to coincide with the bone and muscle trait precision study by Johnston et al., [33]. For boundary delineation, semi-automatic region growing and subject-specific thresholds (via HMH) were used with manual corrections applied as needed [33].

CC (A_{musc}) and IntraMAT area ($A_{IntraMAT}$) at the upper thigh for the four functional muscle groups, as per the guidelines established by Ogawa et al [35]. Using custom algorithms (Matlab), the segmentations were imposed onto the original MR slice and subject-specific thresholds (via HMH) were used to differentiate between muscle and adipose tissue (Figure 5-1) [35,142]. Muscle area was defined as the number of pixels below the threshold (lean muscle) multiplied by pixel size. Similarly, IntraMAT area was defined as the number of pixels above the muscle-adipose tissue threshold multiplied by pixel size.

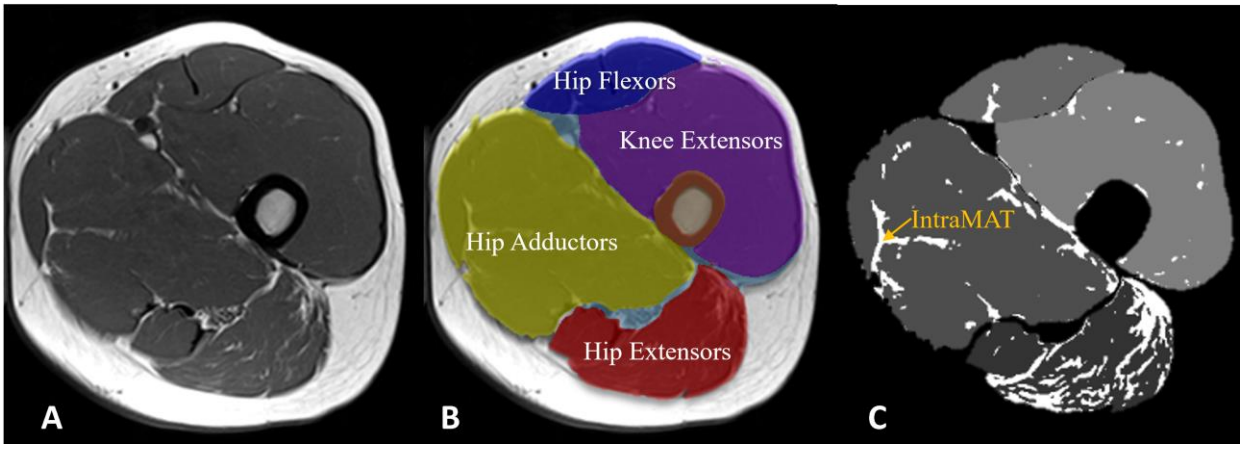

Figure 5-1. Illustration of the muscle and adipose tissue analysis process. A: Raw MRI slice approximately 2 cm below the lesser trochanter; B: Overlay of the segmented muscle groups onto the original MR slice (red: hip extensors; purple: knee extensors; dark blue: hip flexors; yellow: hip adductors; light blue: entire ROI; orange: cortical bone); C: Cross-section of the separated functional muscle groups (greyscale) with the IntraMAT emphasized in white (high intensity)

5.3.4 IntraMAT Precision

We additionally investigated the short-term *in vivo* precision error of the IntraMAT measures at the upper thigh using $CV\%_{RMS}$. To assess the precision, we used the MR scans of the 13 study participants (each scanned 3 times) from Chapter 4; for a total of 39 scans with 26 degrees of freedom [112]. Accordingly, the degrees of freedom establish a reliable precision with an upper 90% confidence limit less than ~31% [112]. We report mean values for each measurement for numerical comparisons. The short-term precision was also assessed in absolute terms using the root mean square standard deviation (SD_{RMS}) of the differences between the 3 repeat measures.

The *in vivo* precision error of area measurements at the upper thigh using MRI are shown in Table 5-2. Precision errors of the A_{musc} measures ranged from 0.82% to 7.04% (mean: 2.11%). For the $A_{IntraMAT}$ measures, precision errors ranged from 6.79% to 22.2% (mean: 11.7%).

Table 5-2. Precision results for the muscle and IntraMAT area measurements at the upper thigh using MRI

Property	Muscle Group	Mean [mm^2]	SD_{RMS}	$CV\%_{RMS}$
A_{musc}	Hip Extensors	2076.3	124.0	7.0%
	Hip Adductors	5109.6	68.2	0.8%
	Hip Flexors	1539.1	22.6	0.9%
	Knee Extensors	2076.3	53.3	1.0%
	Total	3704.3	164.2	0.8%
$A_{IntraMAT}$	Hip Extensors	766.6	106.8	10.2%
	Hip Adductors	373.9	35.9	6.8%
	Hip Flexors	49.1	15.9	22.2%
	Knee Extensors	153.0	27.4	12.2%
	Total	1342.7	146.7	7.1%

5.3.5 Statistical Analysis

Before assessing relationships between muscle and FE derived failure load, we first tested data normality using standardized skewness (standardized skewness = skewness statistic / standard

error of the skewness statistic, with values >-3.29 and <3.29 confirming normality). As the outcomes exhibited normal distributions, we used Pearson correlations to measure the strength of association between the muscle and fat areas with failure loads. We also assessed relationships of participant characteristics (sex, age, weight, height, body mass index [BMI]) with the muscle properties and failure load. Statistical significance was set at $p < 0.01$. All statistical analyses were conducted using IBM SPSS Statistics 25.0 (Chicago, IL, USA).

5.4 Results

5.4.1 Muscle Area Associations

For the fall and stance configuration, significant Pearson correlation coefficients ranged from 0.385 to 0.672 (Table 5-3). For the fall configuration, muscle properties were most strongly associated with the failure load at the neck region. In terms of specific muscles, the hip adductor and total muscle measure offered the strongest correlations with fall failure load. For the stance configuration, muscle properties were strongly associated with failure load at the neck, intertrochanteric, and shaft regions. Conversely, the hip extensor measure offered the weakest correlations. In terms of specific muscles, the hip flexors and total muscle measure offered the strongest correlations with stance failure load. Muscle area was more strongly related to the stance failure load than the fall failure load.

Table 5-3. Pearson correlation coefficients between von Mises stress failure load and muscle area measures. Regional significant associations are highlighted in the table ($p < 0.01$).

Orientation	Region	*Muscle Area*				
		Hip Extensor	**Hip Adductor**	**Hip Flexor**	**Knee Extensor**	**Total**
Fall	Neck	0.323	0.508	0.506	0.484	0.537
	Intertrochanteric	0.273	0.457	0.342	0.353	0.416
	Shaft	0.262	0.365	0.239	0.262	0.328
Stance	Neck	0.385	0.457	0.488	0.487	0.520
	Intertrochanteric	0.372	0.515	0.477	0.467	0.518
	Shaft	0.609	0.591	0.672	0.604	0.671

5.4.2 IntraMat Area Associations

For the fall and stance configuration, significant Pearson correlation coefficients for IntraMAT area ranged from 0.392 to 0.494 (Table 5-4). For the fall configuration, significant IntraMAT properties and failure load correlations were sparser than the muscle properties (Table 5-3). IntraMat was more strongly associated with stance failure load, although the correlations were sporadic (Table 5-4). Generally, the knee extensors and total area measures offered strong associations with failure load. Conversely, the hip extensors and hip adductors did not have significant associations.

Table 5-4. Pearson correlation coefficients between von Mises stress failure load and IntraMAT area measures. Regional significant associations are highlighted in the table ($p < 0.01$).

Orientation	Region	*IntraMAT Area*				
		Hip Extensor	**Hip Adductor**	**Hip Flexor**	**Knee Extensor**	**Total**
Fall	Neck	0.312	0.276	0.418	0.428	0.409
	Intertrochanteric	0.213	0.064	0.137	0.157	0.235
	Shaft	0.131	-0.104	-0.012	0.059	0.111
Stance	Neck	0.352	0.220	0.267	0.377	0.422
	Intertrochanteric	0.232	0.244	0.114	0.394	0.317
	Shaft	0.302	0.258	0.154	0.494	0.392

5.4.3 Participant Characteristics

Correlations were present between muscle and IntraMAT areas with participant characteristics, as shown in Table 5-5. Men had significantly larger muscle area (all groups) than women. Muscle area (all groups) were positively associated with weight and height, with correlation coefficients ranging from 0.476 to 0.615 ($p < 0.05$). IntraMAT area measures were more sporadically associated with participant characteristics. In terms of participant characteristics, weight generally offered the strongest associations with fall and stance failure load whereas sex offered the weakest (Table 5-6). Age was also strongly associated with the failure loads at all three regions.

Table 5-5. Pearson correlation coefficients between the muscle and IntraMAT areas with participant characteristics. Significant associations are highlighted in the table ($p < 0.01$).

Property	**Muscle Group**	*Participant Characteristics*				
		Sex	**Age**	**Weight**	**Height**	**BMI**
A_{musc}	Hip Extensor	0.763	0.180	0.326	0.547	0.089
	Hip Adductor	0.688	0.234	0.478	0.579	0.253
	Hip Flexor	0.793	0.220	0.476	0.613	0.217
	Knee Extensor	0.680	0.299	0.516	0.557	0.288
	Total	0.763	0.271	0.503	0.615	0.251
$A_{IntraMAT}$	Hip Extensor	0.139	0.233	0.573	0.028	0.623
	Hip Adductor	0.257	0.283	0.181	0.453	-0.013
	Hip Flexor	0.135	0.216	0.403	0.209	0.276
	Knee Extensor	0.545	0.356	0.372	0.527	0.110
	Total	0.222	0.330	0.602	0.194	0.555

Table 5-6. Pearson correlation coefficients between the muscle and IntraMAT areas with von Mises stress failure load. Regional significant associations are highlighted in the table ($p < 0.01$).

Orientation	Region	*Participant Characteristics*				
		Sex	**Age**	**Weight**	**Height**	**BMI**
Fall	Neck	0.297	0.558	0.658	0.518	0.478
	Intertrochanteric	0.137	0.408	0.465	0.353	0.370
	Shaft	-0.015	0.386	0.448	0.223	0.500
Stance	Neck	0.306	0.528	0.548	0.583	0.304
	Intertrochanteric	0.303	0.495	0.449	0.645	0.195
	Shaft	0.478	0.487	0.491	0.600	0.241

5.5 Discussion

This study explored the associations between surrounding upper-thigh properties (lean muscle and IntraMAT) and proximal femoral MR-FE derived failure load. This study complements existing muscle-bone interaction studies at the proximal femur [105,133,151], and offers an indication of specific muscular groups which contribute to proximal femoral bone strength. To the best of our knowledge, this is the first study to assess relationships between specific muscle properties and FE-derived estimates of proximal femoral failure load under stance and fall configurations.

The strongest associations between muscle properties (muscle and IntraMAT) and failure load were found at the shaft under a stance configuration, supporting the premise that the femur primarily adapts to the habitually weight-bearing direction [16,44,56]. Study findings support those of Lang et al. who found no change from the baseline failure load (fall configuration with von Mises stress failure criteria) as part of a physical activity intervention study looking at the proximal femurs response to muscle loading [133]. Specifically a significant difference (9% increase, $p < 0.05$) in failure load was only observed for the stance orientation [133]. However, based on the observed positive relationship, increased size of the hip adductor muscle, as well as adjacent muscles, are associated with a higher failure load for the fracture-prone neck and

trochanteric regions under both fall and stance configurations. Accordingly, it is possible that the activities studied by Lang et al. [133], did not markedly affect the hip adductor muscle, which is a direction for future research.

Of interest in this study, FE derived failure loads were most strongly associated with the muscle area while IntraMAT area measurements had fewer and weaker relations for both configurations. This was surprising as we expected high IntraMAT area to be associated with lower failure loads. Conflicting results may be due to the relatively young sample, with high IntraMAT area not necessarily indicating reduced muscle area. In a complimentary analysis between muscle and IntraMAT area (Appendix C), observed associations between hip bone strength and fat area appear to be due to physical size (i.e., larger individuals will have stronger bones, more muscle and more fat). Poor associations may also be due to high error, with low IntraMAT presence leading to poor precision errors. Specifically, the hip flexor's have the lowest IntraMAT precision, with a measurement error ($CV\%_{RMS}$) of 22%. Postulations aside, our findings suggest that IntraMAT presence is associated with greater proximal femoral failure load. These results are in partial agreement with the study by Lang et al., where they found that hip fracture subjects (mean age: 74.7, SD: 5.9) have lower fat area ($p < 0.0001$) than controls [152]. Though, as adipose tissue typically replaces muscle with age [59], IntraMAT area and failure load may be negatively associated in a sample older than the one studied here.

This research has several unique strengths which require consideration. First, we differentiated the upper thigh region into four functional muscle groups and considered muscle and IntraMat area measures. Past studies predominantly focused on cumulative cross-sectional areas exclusively. Our approach allowed us to assess the relationship between each component individually and identify the strongest predictor. Second, we report the associations of FE failure

load and muscle properties at three clinically relevant regions [42,149] for the two commonly studied loading configurations used in literature [103]. The inclusion of different regions and loading configurations may provide insight and direction for prevention strategies aimed at particular sites/muscle groups.

This research has several unique limitations which require consideration. First, the participants (mean age: 30.0, SD: 2.1 years) were relatively young adults. This limitation restricts the generalizability of the precision errors and associations beyond this age group. A complementary association study with older adults is needed for comparison. Second, due to the poor signal-to-noise ratios on some scans, it was difficult to identify the periosteal surface within the greater trochanteric region. To address this, we applied a bias field correction to reduce image inhomogeneity [96,139,140], defined the boundary using semi-automatic region growing and subject-specific thresholds (HMH) [141], and manually corrected segmentations where needed for anatomically correct delineation. Operator judgment though had a large effect on femoral segmentations and may have induced error into the analysis. Thirdly, due to the large slice thickness (4mm), the true 3D geometry of the femur was difficult to capture and resulted in a jagged structure. The large slice thickness may have resulted in the under/over estimation association between failure load and muscle properties. To more accurately characterize the shape of the proximal femur, our original scans consisting of 37 slices were interpolated to 329 slices. This approach led to a more correct shape, but small variations in material properties were not captured, especially within the geometrically complex neck and trochanteric regions. The femoral shaft is less affected by the large slice thickness due to the relatively simpler geometry. As shown in Appendix B, the potentially more trustworthy femoral shaft may be used as the sole measure to estimate failure load of the hip due to high associations with neck and intertrochanteric regions.

5.6 Conclusion

This study found strong associations between hip adductor muscle area, as well as the total surrounding muscle area, on failure load of the fracture-prone neck and intertrochanteric regions under both fall and stance configurations. For the shaft, strong associations between knee extensor, hip flexor, hip adductor, muscle area were found for failure load in the stance configuration. Strongest correlations were noted for the stance configuration, most likely reflective of habitual loading patterns. Results indicate sporadic associations between IntraMAT area and proximal femoral failure; though, associations were positive, suggesting that adiposity is not associated with reduced femoral bone strength (as commonly surmised). Our results may provide insight and direction for prevention strategies aiming to reduce the risk of fracture.

CHAPTER 6
INTEGRATED DISCUSSION

6.1 Overview of Findings

MR-FE is an imaging-based analysis tool that can be used to evaluate strength at the fracture-prone proximal femur. Overcoming the limitations of DXA and QCT-FE based strength characterization, MR-FE is a non-invasive method which is able to distinguish between cortical and trabecular bone and does not expose an individual to harmful ionizing radiation. To our knowledge, this is the first study to report the *in vivo* precision error of MR-FE outcomes at the hip for fall and stance loading configurations. This is also the first study to assess associations of upper-thigh muscle and IntraMAT area with MR-FE derived failure load.

A key achievement of **Chapter 4 – MR-FE Modeling of the Proximal Femur: An *in vivo* Precision Study** is that we found that MR-FE outcomes of the proximal femur have short-term *in vivo* average precision errors <12%. We found that stress and strain outcomes had similar precision (3.3% to 12%), as did the commonly used failure load theories (6.0 to 9.5%). Precision errors were similar between the femoral neck (mean $CV\%_{RMS}$ <7.6%), intertrochanteric (mean $CV\%_{RMS}$ < 7.5%), and shaft regions (mean $CV\%_{RMS}$ < 7.7%). Our results show that MR-FE outcomes are a promising non-invasive technique for monitoring femoral strength *in vivo*.

A key achievement of **Chapter 5 – Association of Muscle and Fat Properties with MR-FE Derived Failure Loads of the Proximal Femur** is that we found hip adductor muscle area and total muscle area to be strongly correlated with failure load of the fracture-prone neck and intertrochanteric region under both fall and stance loading. We also found knee extensor, hip flexor, and hip adductor area to be strongly correlated with failure load of the shaft under stance loading. We also found that failure load of the proximal femur was sporadically associated with IntraMAT area. Though, associations with IntraMAT area were positive, indicating that fat

presence does not lead to weaker bones, as commonly surmised. Study results may provide insight and direction for prevention strategies aiming to reduce the risk of fracture.

6.2 Conclusions

i. MR-FE analyses of the proximal femur can be applied to estimate bone strength. Precision errors of MR-FE derived stress/strain outcomes and failure loads were less than 11.8% for the two loading configurations. Regional MR-FE precision errors ranged from 5.4% to 9.9% for the neck, 4.8% to 11.5% for the intertrochanteric, and 3.31% to 11.8% for the shaft region. Results from this study indicate that MR-FE outcomes have the potential to precisely assess hip strength *in vivo*.

ii. Soft tissue properties at the upper thigh were associated with proximal femur MR-FE failure load outcomes.

    a. Hip adductor muscle area and total muscle area were correlated with failure load of the fracture-prone neck and intertrochanteric region under both fall and stance loading. Hip adductor, hip flexor, and knee extensor area were correlated with failure load of the shaft under stance loading.

    b. Intramuscular fat area was sporadically associated with proximal femoral failure load, and all associations were positive. The common presumption that increased fat presence indicates a lower failure load was not supported by this study.

6.3 Contributions

This thesis research has several contributions which may lead to improved characterization of hip strength and aid in developing fracture prevention strategies. Contributions include:

i. First study to assess the *in vivo* precision error of MR-FE outcomes for fall and stance loading configurations at the hip.

ii. First study to report relationships between upper-thigh muscle and fat areas with failure loads of the proximal femur.

6.4 Clinical Significance

The findings of this thesis provided further evidence that MR-FE models can be used to assess femoral strength *in vivo*. Our research suggests that MRI can be used to monitor changes in bone strength as well as muscle, thereby acting as a diagnostic imaging tool which may assist in reducing fracture occurrence rates. Additionally, this research provides a new tool to study muscle-bone relationships at the hip. An understanding of the relationship between muscle properties (muscle and IntraMAT) and failure load may assist in future proximal femur strength assessment and development of preventative strategy developments.

6.5 Future Research

i. Precision was calculated for six different MR-FE mechanical measures and five different failure criteria; however, it is unclear whether these outcomes accurately represent the true mechanical behaviour of the proximal femur. MR-FE outcomes may be validated using experimental testing of the proximal femur.

ii. MR-FE outcomes were related to muscle and IntraMAT properties at the upper-thigh; however, it is unclear how participant activity data (athletic loading history, jump height, etc.) may additionally be related. Future studies may include additional participant data for evaluation of the associations.

iii. In this thesis, a single elastic moduli equation was used for cortical and trabecular bone. Cortical-specific and trabecular-specific relationships could be used to map the elastic modulus of each voxel and may improve accuracy. This needs to be assessed in a future validation study.

iv. In the precision and association studies, relatively young adult populations were studied. It is unclear how the results from this thesis would differ beyond this age group. A future study with older adult participants is needed.

REFERENCES

1. McGlasson R, Zellermeyer V, MacDonald V, Spafford D, Mcmullan JL, Lo N, et al. National Hip Fracture Toolkit. Waddell J, editor. 2011.
2. Cummings SR, Melton LJ. Osteoporosis I: Epidemiology and outcomes of osteoporotic fractures. Lancet. 2002;359(9319):1761–7.
3. Carpintero P. Complications of hip fractures: A review. World J Orthop [Internet]. 2014;5(4):402. Available from: http://www.wjgnet.com/2218-5836/full/v5/i4/402.htm
4. Deal CL. Osteoporosis: prevention, diagnosis, and management. Am J Med. 1997;102(1A):35–9.
5. Tinetti M, Speechley M, Ginter S. Risk Factors for Falls Among Elderly Persons Living in the Community. N Engl J Med. 1985;319(26):1701–7.
6. Kanis JA, Seeman E, Johnell O, Rizzoli R, Delmas P. The perspective of the International Osteoporosis Foundation on the official positions of the International Society for Clinical Densitometry. Osteoporos Int. 2005;16(5):456–9.
7. Marshall D, Johnell O, Wedel H. Meta-analysis of how well measures of bone mineral density predict occurrence of osteoporotic fractures. Br Med J. 1996;312(7041):1254–9.
8. Geusens P, van Geel T, van den Bergh J. Can hip fracture prediction in women be estimated beyond bone mineral density measurement alone? Ther Adv Musculoskelet Dis. 2010;2(2):63–77.
9. Schott AM, Cormier C, Hans D, Favier F, Hausherr E, Delmas PD. International Original Article How Hip and Whole-Body Bone Mineral Density Predict Hip Fracture in Elderly Women : The EPIDOS Prospective Study. Osteoporos Int. 1998;8:247–54.
10. Rajapakse CS, Hotca A, Newman BT, Ramme A, Kobe EA. Patient-specific hip Fracture

strength assessment with Microstructural MR imaging– based Finite element Modeling. Radiology. 2017;283(3):854–61.

11. Hwang SN, Wehrli FW. Estimating voxel volume fractions of trabecular bone on the basis of magnetic resonance images acquired in vivo. Int J Imaging Syst Technol. 1999;10(2):186–98.
12. Ferretti JL, Cointry GR, Capozza RF, Frost HM. Bone mass, bone strength, muscle-bone interactions, osteopenias and osteoporoses. Mech Ageing Dev. 2003;124(3):269–79.
13. Frost HM. The mechanostat: a proposed pathogenetic mechanism of osteoporoses and the bone mass effects of mechanical and nonmechanical agents. Bone Miner. 1987;2(2):73–85.
14. Mellon SJ, Tanner KE. Bone and its adaptation to mechanical loading: A review. Int Mater Rev. 2012;57(5):235–55.
15. Digirolamo DJ, Kiel DP, Esser KA. Bone and skeletal muscle: Neighbors with close ties. J Bone Miner Res. 2013;28(7):1509–18.
16. Ireland A, Rittweger J, Degens H. The influence of muscular action on bone strength via exercise. Clin Rev Bone Miner Metab. 2014;12(2):93–102.
17. Frank H, Netter M. Atlas of Human Anatomy. 6th Editio. Vol. 6. Philadelphia, PA, USA: Saunders, an imprint of Elsevier Inc; 2014.
18. Martini F, Timmons M, Tallitsch R. Human Anatomy. 8th Editio. London, United Kingdom: Pearson Education; 2014. 233–261 p.
19. Foran J, Fischer S. OrthoInfo: Total Hip Replacement. American Academy of Orthopedic Surgeons. 2019.
20. Metcalfe D. The pathophysiology of osteoporotic hip fracture. McGill J Med. 2008;11(1):51–7.

21. Lunn DE, Lampropoulos A, Stewart TD. Anatomy & Biomechanics of the Hip. Open Sport Med J. 2016;30(3):239–46.

22. Kim Y-H (Department of OS. Acetabular Dysplasia and Osteoarthritis Developed by an Eversion of the Acetabular Labrum. Yonsei Med J. 1984;25(2):97–104.

23. Mansfield PJ, Neumann D. Essentials of Kinesiology for the Physical Therapist Assistant. 3rd ed. Maryland Heights, Missouri: Mosby; 2019. 1–403 p.

24. Boymans TAEJ, Veldman HD, Noble PC, Heyligers IC, Grimm B. The Femoral Head Center Shifts in a Mediocaudal Direction During Aging. J Arthroplasty. 2017;32(2):581–6.

25. Rudman KE, Aspden RM, Meakin JR. Compression or tension? The stress distribution in the proximal femur. Biomed Eng Online. 2006;5:1–7.

26. Choi WJ, Cripton PA, Robinovitch SN. Effects of hip abductor muscle forces and knee boundary conditions on femoral neck stresses during simulated falls. Osteoporos Int. 2014;26(1):291–301.

27. Gray H. Anatomy of the Human Body [Internet]. 20th Ed. Lewis WH, editor. Philadelphia, USA: Lea & Febiger; 1918. Available from: Bartleby.com/107/

28. Martini F, Timmons M, Tallitsch R. Human Anatomy. 7th Ed. Berriman L, Seibel K, editors. Glenview (Illinois): Pearson Education; 2012.

29. Beck TJ, Oreskovic TL, Stone KL, Ruff CB, Ensrud K, Nevitt MC, et al. Structural adaptation to changing skeletal load in the progression toward hip fragility: the study of osteoporotic fractures. J Bone Miner Res. 2001;16(6):1108–19.

30. Pearson OM, Lieberman DE. The aging of Wolff's "law": Ontogeny and responses to mechanical loading in cortical bone. Yearb Phys Anthropol. 2004;47:63–99.

31. Avin KG, Bloomfield SA, Warden SJ. Biomechanical Aspects of the Muscle-Bone

Interaction. Curr Osteoporos Rep. 2015;13(1):1–8.

32. Lu T, Stephen T, O'Connor J, Walker P. Influence of Muscle Activity on the Forces in the Femur: An IN VIVO Study. J Biomech. 1997;30(97):1101–6.

33. Johnston JD, Liao L, Dolovich AT, Leswick DA, Kontulainen SA. Magnetic resonance imaging of bone and muscle traits at the hip: An in vivo precision study. J Musculoskelet Neuronal Interact. 2014;14(1):104–10.

34. Vettor R, Milan G, Franzin C, Sanna M, De Coppi P, Rizzuto R, et al. The origin of intermuscular adipose tissue and its pathophysiological implications. AJP Endocrinol Metab. 2009;297(5):E987–98.

35. Ogawa M, Lester R, Akima H, Gorgey AS. Quantification of intermuscular and intramuscular adipose tissue using magnetic resonance imaging after neurodegenerative disorders. Neural Regen Res. 2017;12(12):2100–5.

36. Nawathe S, Nguyen BP, Barzanian N, Akhlaghpour H, Bouxsein ML, Keaveny TM. Cortical and trabecular load sharing in the human femoral neck. J Biomech [Internet]. 2015;48(5):816–22. Available from: http://dx.doi.org/10.1016/j.jbiomech.2014.12.022

37. Zioupos P, Currey JD. The extent of microcracking and the morphology of microcracks in damaged bone. J Mater Sci. 1994;29(4):978–86.

38. de Bakker PM, Manske SL, Ebacher V, Oxland TR, Cripton PA, Guy P. During sideways falls proximal femur fractures initiate in the superolateral cortex: Evidence from high-speed video of simulated fractures. J Biomech. 2009;42(12):1917–25.

39. Panula J, Pihlajamäki H, Mattila VM, Jaatinen P, Vahlberg T, Aarnio P, et al. Mortality and cause of death in hip fracture patients aged 65 or older - a population-based study. BMC Musculoskelet Disord. 2011;12(1):105.

40. Zuckerman J. Hip Fracture. N Engl J Med. 1996;334(23):1519–25.

41. Miller W. Survival and ambulation following hip fracture. J Bone Jt Surg. 1978;60(7):930–4.

42. Sheehan SE, Shyu JY, Weaver MJ, Sodickson AD, Khurana B. Proximal Femoral Fractures: What the Orthopedic Surgeon Wants to Know. RadioGraphics. 2015;35(5):1624–1624.

43. Parkkari J, Kannus P, Palvanen M, Natri A, Vainio J, Aho H, et al. Majority of hip fractures occur as a result of a fall and impact on the greater trochanter of the femur: a prospective controlled hip fracture study with 206 consecutive patients. Calcif Tissue Int. 1999;65:183–7.

44. Fuchs RK, Kersh ME, Carballido-gamio J, Thompson WR, Keyak JH, Warden SJ. Physical activity for strengthening fracture prone regions of the proximal femur. Curr Osteoporos Rep. 2018;15(1):43–52.

45. Keyak JH, Rossi SA, Jones KA, Les CM, Skinner HB. Prediction of fracture location in the proximal femur using finite element models. Med Eng Phys. 2001;23(9):657–64.

46. Keyak JH. Improved prediction of proximal femoral fracture load using nonlinear finite element models. Med Eng Phys. 2001;23(3):165–73.

47. Lotz J, Cheal E, Hayes W. Stress distributions within the proximal femur during gait and falls: implications for osteoporotic fracture. Osteoporos Int. 1995;5(4):252–61.

48. Zani L, Erani P, Grassi L, Taddei F, Cristofolini L. Strain distribution in the proximal Human femur during in vitro simulated sideways fall. J Biomech. 2015;48(10):2130–43.

49. Pinilla TP, Boardman KC, Bouxsein ML, Myers ER, Hayes WC. Impact direction from a fall influences the failure load of the proximal femur as much as age-related bone loss. Calcif Tissue Int. 1996;58(4):231–5.

50. Courtney AC, Wachtel EF, Myers ER, Hayes WC. Effects of loading rate on strength of the proximal femur. Calcif Tissue Int. 1994;55(1):53–8.

51. Keyak JH. Relationships between femoral fracture loads for two load configurations. J Biomech. 2000;33:499–502.

52. Pottecher P, Engelke K, Duchemin L, Museyko O, Moser T, Mitton D, et al. Prediction of hip failure load: In vitro study of 80 femurs using three imaging methods and finite element models-the european fracture study (EFFECT). Radiology. 2016;280(3):837–47.

53. Grisso J, Kelsey JL, Strom B, Chiu G, O'Brien L, Hoffman S, et al. Risk Factors for Falls as a Cause of Hip Fractures in Women. N Engl J Med. 1991;324(19):1326–31.

54. Chen H, Zhou X, Fujita H, Onozuka M, Kubo K. Age-Related Changes in Trabecular and Cortical Bone Microstructure. Int J Endocrinol. 2013;2013:1–9.

55. Krug R, Burghardt A, Majumander S, Link T. High-resolution Imaging Techniques for the Assessment of Osteoporosis. Radial Clin North Am. 2010;48(3):601–21.

56. Hart NH, Nimphius S, Rantalainen T, Ireland A, Siafarikas A, Newton RU. Mechanical basis of bone strength: Influence of bone material, bone structure and muscle action. J Musculoskelet Neuronal Interact. 2017;17(3):114–39.

57. LaStayo PC, Ewy GA, Pierotti DD, Johns RK, Lindstedt S. The Positive Effects of Negative Work: Increased Muscle Strength and Decreased Fall Risk in a Frail Elderly Population. Journals Gerontol Ser A Biol Sci Med Sci. 2003;58(5):M419–24.

58. Russo CR. The effects of exercise on bone. Basic concepts and implications for the prevention of fractures. Clin Cases Miner Bone Metab. 2009;6(3):223–8.

59. Lang T, Cauley JA, Tylavsky F, Bauer D, Cummings S, Harris TB. Computed tomographic measurements of thigh muscle cross-sectional area and attenuation coefficient predict hip

fracture: The health, aging, and body composition study. J Bone Miner Res. 2010;25(3):513–9.

60. Addison O, Young P, Inacio M, Bair W-N, Prettyman MG, Beamer BA, et al. Hip but Not Thigh Intramuscular Adipose Tissue is Associated with Poor Balance and Increased Temporal Gait Variability in Older Adults HHS Public Access. Curr Aging Sci. 2014;7(2):137–43.

61. Orwoll ES, Marshall LM, Nielson CM, Cummings SR, Lapidus J, Cauley JA, et al. Finite element analysis of the proximal femur and hip fracture risk in older men. J Bone Miner Res. 2009;24(3):475–83.

62. Small RE. Uses and limitations of bone mineral density measurements in the management of osteoporosis. MedGenMed. 2005;7(2):1–12.

63. Rolland Y, Abellan van Kan G, Bénétos A, Blain H, Bonnefoy M, Chassagne P, et al. Frailty, osteoporosis and hip fracture: causes, consequences and therapeutic perspectives. J Nutr Health Aging. 2008;12(5):335–46.

64. Lou Bonnick S. HSA: Beyond BMD with DXA. Bone. 2007;41:9–12.

65. Schuit SCE, Van Der Klift M, Weel AEAM, De Laet CEDH, Burger H, Seeman E, et al. Fracture incidence and association with bone mineral density in elderly men and women: The Rotterdam Study. Bone. 2004;34(1):195–202.

66. Beck TJ. Extending DXA beyond bone mineral density: Understanding hip structure analysis. Curr Osteoporos Rep. 2007;5(2):49–55.

67. Kaptoge S, Beck TJ, Reeve J, Stone KL, Hillier TA, Cauley JA, et al. Prediction of incident hip fracture risk by femur geometry variables measured by hip structural analysis in the study of osteoporotic fractures. J Bone Miner Res. 2008;23(12):1892–904.

68. Khoo BCC, Beck TJ, Qiao QH, Parakh P, Semanick L, Prince RL, et al. In vivo short-term precision of hip structure analysis variables in comparison with bone mineral density using paired dual-energy X-ray absorptiometry scans from multi-center clinical trials. Bone. 2005;37(1):112–21.

69. Helgason B, Perilli E, Schileo E, Taddei F, Brynjólfsson S, Viceconti M. Mathematical relationships between bone density and mechanical properties: A literature review. Clin Biomech. 2008;23(2):135–46.

70. Johannesdottir F, Poole KES, Reeve J, Siggeirsdottir K, Aspelund T, Mogensen B, et al. Distribution of Cortical Bone in the Femoral Neck and Hip Fracture: A Prospective Case-Control Analysis of 143 Incident Hip Fractures. Bone. 2011;48(6):1268–76.

71. Lang TF. Quantitative Computed Tomography. Radiol Clin North Am. 2010;48(3):589–600.

72. Ito M, Nakamura T, Fukunaga M, Shiraki M, Matsumoto T. Effect of eldecalcitol, an active vitamin D analog, on hip structure and biomechanical properties: 3D assessment by clinical CT. Bone. 2011;49(3):328–34.

73. Zebaze RMD, Jones A, Welsh F, Knackstedt M, Seeman E. Femoral neck shape and the spatial distribution of its mineral mass varies with its size: Clinical and biomechanical implications. Bone. 2005;37(2):243–52.

74. Carpenter RD, Sigurdsson S, Zhao S, Lu Y, Eiriksdottir G, Sigurdsson G, et al. Effects of Age and Sex on the Strength and Cortical Thickness of the Femoral Neck. Bone. 2011;48(4):741–7.

75. Biswas D, Bible JE, Bohan M, Simpson AK, Whang PG, Grauer JN. Radiation exposure from musculoskeletal computerized tomographic scans. J Bone Jt Surg - Ser A.

2009;91(8):1882–9.

76. Pitman AG, Budd RS, Mckenzie AF. Radiation dose in computed tomography of the pelvis : Comparison of helical and axial scanning. Diagnostic Radiol. 1997;41:329–35.

77. Damilakis J, Adams JE, Guglielmi G, Link TM. Radiation exposure in X-ray-based imaging techniques used in osteoporosis. Eur Radiol. 2010;20(11):2707–14.

78. Rossi A, Zoico E, Goodpaster BH, Sepe A, Di Francesco V, Fantin F, et al. Quantification of intermuscular adipose tissue in the erector spinae muscle by MRI: Agreement with histological evaluation. Obesity. 2010;18(12):2379–84.

79. Currie S, Hoggard N, Craven IJ, Hadjivassiliou M, Wilkinson ID. Understanding MRI: basic MR physics for physicians. Postgrad Med J. 2013;89(1050):209–23.

80. Maden-Wilkinson TM, Degens H, Jones DA, McPhee JS. Comparison of MRI and DXA to measure muscle size and age-related atrophy in thigh muscles. J Musculoskelet Neuronal Interact. 2013;13(3):320–8.

81. Karampinos D, Baum T, Nardo L, Hamza A, Yu H, Carballido-Gamio J, et al. Characterization of the regional distribution of skeletal muscle adipose tissue in type 2 diabetes using chemical shift-based water/fat separation. J Magn Reson Imaging. 2012;35(4):899–907.

82. Abe S, Narra N, Nikander R, Hyttinen J, Kouhia R, Sievänen H. Impact loading history modulates hip fracture load and location : A finite element simulation study of the proximal femur in female athletes. J Biomech. 2018;76:136–43.

83. Wehrli FW. Structural and functional assessment of trabecular and cortical bone by micro magnetic resonance imaging. J Magn Reson Imaging. 2007;25(2):390–409.

84. Bauer JS, Link TM. Advances in Osteoporosis Imaging. Eur J Radiol. 2009;71(3):440–9.

85. Gibson LJ. The mechanical behaviour of cancellous bone. J Biomech. 1985;18(5):317–28.

86. Sievänen H, Karstila T, Apuli P, Kannus P. Magnetic resonance imaging of the femoral neck cortex. Acta radiol. 2007;48(3):308–14.

87. Gomberg BR, Saha PK, Wehrli FW. Method for cortical bone structural analysis from magnetic resonance images. Acad Radiol. 2005;12(10):1320–32.

88. Bouxsein ML. Determinants of skeletal fragility. Best Pract Res Clin Rheumatol. 2005;19(6):897–911.

89. Manske SL, Liu-Ambrose T, De Bakker PM, Liu D, Kontulainen S, Guy P, et al. Femoral neck cortical geometry measured with magnetic resonance imaging is associated with proximal femur strength. Osteoporos Int. 2006;17(10):1539–45.

90. Chacon-Caldera J, Malzacher M, Schad LR. Partially orthogonal resonators for magnetic resonance imaging. Sci Rep. 2017;7:1–8.

91. Uros V, Franjo P, Bostjan L. A review of methods for correction of intensity inhomogeneity in MRI. IEEE Trans Med Imaging. 2007;26(3):405–21.

92. Liang Z, Lauterbur P. Principles of magnetic resonance imaging: a signal processing perspective. New York, NY: IEEE Engineering in Medicine and Biology Society Pres; 2007.

93. Roy S, Carass A, Bazin P-L, Prince JL. Intensity inhomogeneity correction of magnetic resonance images using patches. Med Imaging 2011 Image Process. 2011;7962:79621F.

94. Bridcut R, Redpath T, Gray C, Staff R. The use of SPAMM to assess spatial distortion due to static field inhomogeneity in dental MRI. Phys Med Biol. 2001;46(5):1357–67.

95. Belaroussi B, Milles J, Carme S, Zhu YM, Benoit-Cattin H. Intensity non-uniformity correction in MRI: Existing methods and their validation. Med Image Anal.

2006;10(2):234–46.

96. Tustison NJ, Avants BB, Cook PA, Zheng Y, Egan A, Yushkevich PA, et al. N4ITK: Improved N3 bias correction. IEEE Trans Med Imaging. 2010;29(6):1310–20.

97. Zienkiewicz O, Taylor L. The Finite Element Method. 2nd Editio. Boston: Butterworth-Heinemann; 1991.

98. Keyak JH, Kaneko TS, Tehranzadeh J, Skinner HB. Predicting proximal femoral strength using structural engineering models. Clin Orthop Relat Res. 2005;(437):219–28.

99. Edwards WB, Troy KL. Finite element prediction of surface strain and fracture strength at the distal radius. Med Eng Phys. 2012;34(3):290–8.

100. Engelke K, van Rietbergen B, Zysset P. FEA to Measure Bone Strength: A Review. Clin Rev Bone Miner Metab. 2016;14(1):26–37.

101. Samelson EJ, Broe KE, Xu H, Yang L, Boyd S, Biver E, et al. Cortical and trabecular bone microarchitecture as an independent predictor of incident fracture risk in older women and men in the Bone Microarchitecture International Consortium (BoMIC): a prospective study. Lancet Diabetes Endocrinol. 2019;7(1):34–43.

102. Nawathe S, Akhlaghpour H, Bouxsein ML, Keaveny TM. Microstructural failure mechanisms in the human proximal femur for sideways fall loading. J Bone Miner Res. 2014;29(2):507–15.

103. Keyak JH, Rossi SA. Prediction of femoral fracture load using finite element models : an examination of stress- and strain-based failure theories. J Biomech. 2000;33(2):209–14.

104. Keyak JH, Rossi SA, Jones KA, Skinner HB. Prediction of femoral fracture load using automated finite element modeling. J Biomech. 1998;31.

105. Abe S, Narra N, Nikander R, Hyttinen J, Kouhia R, Sievänen H. Exercise loading history

and femoral neck strength in a sideways fall: A three-dimensional finite element modeling study. Bone. 2016;92:9–17.

106. Gilchrist S, Nishiyama KK, Boyd SK, Guy P, Cripton P. Proximal femur bone strength estimated by a computationally fast finite element analysis in a sideways fall configuration. J Biomech. 2013;46(7):1231–6.

107. Bessho M, Ohnishi I, Okazaki H, Sato W, Kominami H, Matsunaga S, et al. Prediction of the strength and fracture location of the femoral neck by CT-based finite-element method: A preliminary study on patients with hip fracture. J Orthop Sci. 2004;9(6):545–50.

108. Schileo E, Balistreri L, Grassi L, Cristofolini L, Taddei F. To what extent can linear finite element models of human femora predict failure under stance and fall loading configurations? J Biomech. 2014;47(14):3531–8.

109. Qasim M, Farinella G, Zhang J, Li X, Yang L, Eastell R, et al. Patient-specific finite element estimated femur strength as a predictor of the risk of hip fracture: the effect of methodological determinants. Osteoporos Int. 2016;27(9):2815–22.

110. Cody DD, Gross GJ, Hou FJ, Spencer HJ, Goldstein SA, Fyhrie DP. Feomral strength is better predicted by finite element models than QCT and DXA. J Biomech. 1999;32:1013–20.

111. Cody DD, Hou FJ, Divine GW, Fyhrie DP. Short term in vivo precision of proximal femoral finite element modeling. Ann Biomed Eng. 2000;28(4):408–14.

112. Glüer CC, Blake G, Lu Y, Blunt BA, Jergas M, Genant HK. Accurate assessment of precision errors: How to measure the reproducibility of bone densitometry techniques. Osteoporos Int. 1995;5(4):262–70.

113. Lotz JC, Cheal EJ, Hayes WC. Fracture prediction for the proximal femur using finite

element models: Part I- Linear analysis. J Biomech Eng. 1991;113(4):361–5.

114. Chang G, Honig S, Babb JS, Regatte RR. Finite Element Analysis Applied to 3-T MR Imaging of Proximal Femur Microarchitecture : Lower Bone Strength in Patients with Fragility Fractures Compared with Control. Radiology. 2014;272(2).

115. Rajapakse CS, Chang G. Micro-Finite Element Analysis of the Proximal Femur on the Basis of High-Resolution Magnetic Resonance Images. Curr Osteoporos Rep. 2018;16(6):657–64.

116. Chang G, Hotcha-Cho A, Rusinek H, Honig S, Mikheev A, Egol K, et al. Measurement reproducibility of magnetic resonance imaging- based finite element analysis of proximal femur microarchitecture for in vivo assessment of bone strength. Magn Reson Mater Physics, Biol Med. 2015;28(4):407–12.

117. Rajapakse CS, Gupta N, Evans M, Alizai H, Shukurova M, Hong AL, et al. Influence of bone lesion location on femoral bone strength assessed by MRI-based finite-element modeling. Bone. 2019;122(February):209–17.

118. Zhang N, Magland J, Rajapakse CS, Bhagat YA, Wehrli FW. Potential of in vivo MRI-based nonlinear finite-element analysis for the assessment of trabecular bone post-yield properties. Med Phys. 2013;40(5).

119. Öhman C, Baleani M, Pani C, Taddei F, Alberghini M, Viceconti M, et al. Compressive behaviour of child and adult cortical bone. Bone. 2011;49(4):769–76.

120. Schileo E, Dall'Ara E, Taddei F, Malandrino A, Schotkamp T, Baleani M, et al. An accurate estimation of bone density improves the accuracy of subject-specific finite element models. J Biomech. 2008;41(11):2483–91.

121. Nazemi SM, Kalajahi SMH, Cooper DML, Kontulainen SA, Holdsworth DW, Masri BA,

et al. Accounting for spatial variation of trabecular anisotropy with subject-specific finite element modeling moderately improves predictions of local subchondral bone stiffness at the proximal tibia. J Biomech. 2017;59:101–8.

122. Morgan EF, Keaveny TM. Dependence of yield strain of human trabecular bone on anatomic site. J Biomech. 2001;34(5):569–77.

123. Budynas R, Nisbett JK. Shigley's Mechanical Engineering Design. 10th ed. New York, NY: McGraw-Hill Education; 2015. 1–1082 p.

124. Hoffman O. The Brittle Strength of Orthotropic Materials. J Compos Mater. 1967;1(1967):200–6.

125. Nakai R, Azuma T, Sudo M, Urayama S, Takizawa O, Tsutsumi S. MRI analysis of structural changes in skeletal muscles and surrounding tissues following long-term walking exercise with training equipment. J Appl Physiol. 2008;105(3):958–63.

126. Ferrucci L, Baroni M, Ranchelli A, Lauretani F, Maggio M, Mecocci P, et al. Interaction Between Bone and Muscle in Older Persons with Mobility Limitations. Curr Pharm Des. 2014;20(19):3178–97.

127. Tachiki T, Kouda K, Dongmei N, Tamaki J, Iki M, Kitagawa J, et al. Muscle strength is associated with bone health independently of muscle mass in postmenopausal women: the Japanese population-based osteoporosis study. J Bone Miner Metab. 2019;37(1):53–9.

128. Rupaimoole R, Lee J, Haemmerle M, Ling H, Previs RA, Millward NMZ, et al. Mid-thigh cortical bone structural parameters, muscle mass and strength and association with lower limb fractures in older men and women. Calcif Tissue Int. 2012;90(5):354–64.

129. Högler W, Blimkie CJR, Cowell CT, Inglis D, Rauch F, Kemp AF, et al. Sex-specific developmental changes in muscle size and bone geometry at the femoral shaft. Bone.

2008;42(5):982–9.

130. Niinimäki S, Narra N, Härkönen L, Abe S, Nikander R, Hyttinen J, et al. Do bone geometric properties of the proximal femoral diaphysis reflect loading history, muscle properties, or body dimensions? Am J Hum Biol. 2019;31(4):1–13.

131. Correa-de-Araujo R, Harris-Love MO, Miljkovic I, Fragala MS, Anthony BW, Manini TM. The Need for Standardized Assessment of Muscle Quality in Skeletal Muscle Function Deficit and Other Aging-Related Muscle Dysfunctions: A Symposium Report. Front Physiol. 2017;8(FEB):1–19.

132. Schafer AL, Vittinghoff E, Lang TF, Sellmeyer DE, Harris TB, Kanaya AM, et al. Fat infiltration of muscle, diabetes, and clinical fracture risk in older adults. J Clin Endocrinol Metab. 2010;95(11):368–72.

133. Lang TF, Saeed IH, Streeper T, Carballido-Gamio J, Harnish RJ, Frassetto LA, et al. Spatial heterogeneity in the response of the proximal femur to two lower-body resistance exercise regimens. J Bone Miner Res. 2014;29(6):1337–45.

134. Ruan XY, Gallagher D, Harris T, Albu J, Heymsfield S, Kuznia P, et al. Estimating whole body intermuscular adipose tissue from single cross-sectional magnetic resonance images. J Appl Physiol. 2009;102(2):748–54.

135. Glüer CC. Monitoring skeletal change by radiological techniques. J bone Miner Res. 1999;14:1952–62.

136. Beck TJ. Hip structural analysis (HSA) program. Center for Disease Control and Prevention. Baltimore, MD; 2002.

137. Rajapakse CS, Leonard MB, Bhagat YA, Sun W, Magland JF, Wehrli FW. Micro–MR Imaging–based Computational Biomechanics Demonstrates Reduction in Cortical and

Trabecular Bone Strength after Renal Transplantation. Radiology. 2012;262(3):912–20.

138. Roy S, Carass A, Bazin P-L, Prince J. Intensity Inhomogeneity Correction of Magnetic Resonance Images using Patches. Proc SPIE. 2011;7962:1–11.

139. Tustison NJ, Gee JC. N4ITK: Nick's N3 ITK Implementation For MRI Bias Field Correction. InsightJournal. 2009;1–8.

140. Fedorov A., Beichel R., Kalpathy-Cramer J., Finet J., Fillion-Robin J-C., Pujol S., Bauer C., Jennings D., Fennessy F.M., Sonka M., Buatti J., Aylward S.R., Miller J.V., Pieper S. KR. 3D Slicer as an Image Computing Platform for the Quantitative Imaging Network. Magn Reson Imaging. 2012. p. 1323–41.

141. Spoor CF, Zonneveld FW, Macho GA. Linear measurements of cortical bone and dental enamel by computed tomography: Applications and problems. Am J Phys Anthropol. 1993;91(4):469–84.

142. Fajardo RJ, Ryan TM, Kappelman J. Assessing the accuracy of high-resolution X-ray computed tomography of primate trabecular bone by comparisons with histological sections. Am J Phys Anthropol. 2002;118(1):1–10.

143. Frankel VH. The Femoral Neck . Function, Fracture Mechanism, Internal Fixation. An Experimental Study. J Bone Joint Surg Br. 1963;45.

144. Bonneau N, Libourel PA, Simonis C, Puymerail L, Baylac M, Tardieu C, et al. A three-dimensional axis for the study of femoral neck orientation. J Anat. 2012;221(5):465–76.

145. Zysset PK, Edward Guo X, Edward Hoffler C, Moore KE, Goldstein SA. Elastic modulus and hardness of cortical and trabecular bone lamellae measured by nanoindentation in the human femur. J Biomech. 1999;32(10):1005–12.

146. Helgason B, S.Gilchrist, Ariza O, Chak JD, Zheng G, Widmer RP, et al. Development of a

balanced experimental-computational approach to understanding the mechanics of proximal femur fractures. Med Eng Phys. 2014;36(6):793–9.

147. Evans FG, Vincentelli R. Relations of the compressive properties of human cortical bone to histological structure and calcification. J Biomech. 1974;7(1):1–2.

148. Arjmand H, Nazemi M, Kontulainen SA, McLennan CE, Hunter DJ, Wilson DR, et al. Mechanical Metrics of the Proximal Tibia are Precise and Differentiate Osteoarthritic and Normal Knees: A Finite Element Study. Sci Rep. 2018;8(1):11478.

149. Russell G V., Kregor PJ, Jarrett CA, Zlowodzki M. Complicated femoral shaft fractures. Orthop Clin North Am. 2002;33(1):127–42.

150. Baxter-Jones ADG, Kontulainen SA, Faulkner RA, Bailey DA. A longitudinal study of the relationship of physical activity to bone mineral accrual from adolescence to young adulthood. Bone. 2008;43(6):1101–7.

151. Nikander R, Kannus P, Dastidar P, Hannula M, Harrison L, Cervinka T, et al. Targeted exercises against hip fragility. Osteoporos Int. 2009;20(8):1321–8.

152. Lang T, Koyama A, Li C, Li J, Lu Y, Saeed I, et al. Pelvic body composition measurements by quantitative computed tomography: Association with recent hip fracture. Bone. 2008;42(4):798–805.

153. Melton JL, Khosla S, Crowson CS, O'Connor MK, O'Fallon MW, Riggs BL. Epidemiology Sarcopenia. J Am Geriatr Soc. 2000;48:625–30.

154. Holloszy J. The Biology of Aging. Mayo Clin Proc. 2000;75(1).

APPENDIX A: BVF LINEARITY CHECK

We validated that a linear relationship exists between the calculated and known BVF's for our scan parameters and homogeneity corrected images. To test, we created an MR phantom using six jars containing three different solid materials of known BVF's and oil (Figure A-1). Each solid material was placed in a separate jar, fully submerged in canola oil, and then placed in a vacuum chamber for degassing. Specifically, the BVF and materials used for the phantom were:

- 1 x pure canola oil (BVF = 0)
- 1 x solid delrin block (2.2 cm x 2.2 cm x 2.2 cm; BVF = 1)
- 2 x 7.5 PCF rigid open cell block foam (2.2 cm x 2.2 cm x 2.2 cm; BVF = 0.11) (SKU: 1522-507; Sawbones, Vashon, WA)
- 2 x 20 PCF rigid open cell block foam (2.2 cm x 2.2 cm x 2.2 cm; BVF = 0.21) (SKU: 1522-526; Sawbones, Vashon WA)

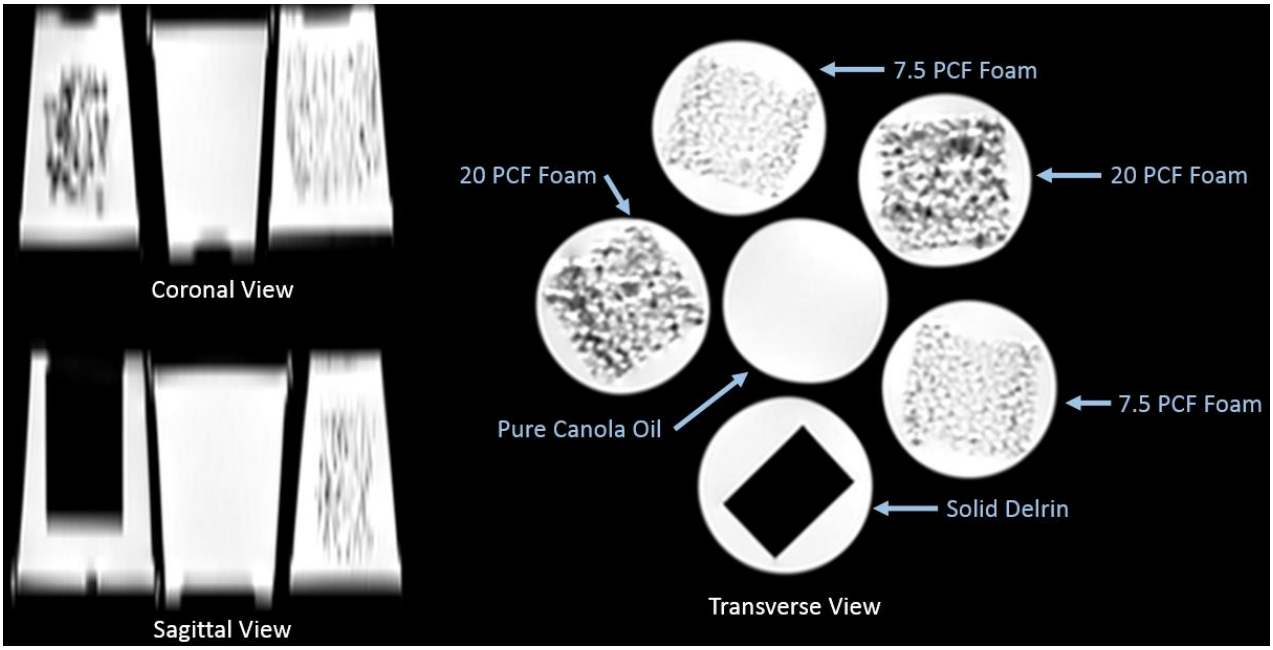

Figure A-1. Coronal, sagittal and transverse views of the MR phantom. The phantom consisted of pure canola oil, delrin, 20 PCF foam, and 7.5 PCF foam.

We scanned the phantom with MRI parameters matching the participant hip scans (T1-weighted turbo spin echo sequence was used with MR scanning parameters: TR 616 ms, TE 12 ms, 2 excitations, 180˚ flip angle, 0.45 x 0.45 mm in plan pixel size, 4 mm slice thickness, ~4.5 minute scan time, ~37 images). The phantom scan was corrected for inhomogeneity [139,140], and then interpolated (cubic) to create an isotropic array using commercial software (Analyze 12.0). To define the phantom materials with known BVF's, each slice of the MR scan was then semi-automatically segmented. Manual corrections were applied to remove lodged air bubbles using commercial software (Analyze 12.0).

Using pure canola oil as the maximum scan intensity, we computed the BVF of each material from the segmentations. Plotting the known BVF's against the calculated BVF's (Figure A-2), it was found that a strong linear relationship exists (coefficient of determination, R^2 = 0.9995). Results confirmed that the linear relationship used to compute BVF from the MRI intensities remained true following the inhomogeneity correction [11].

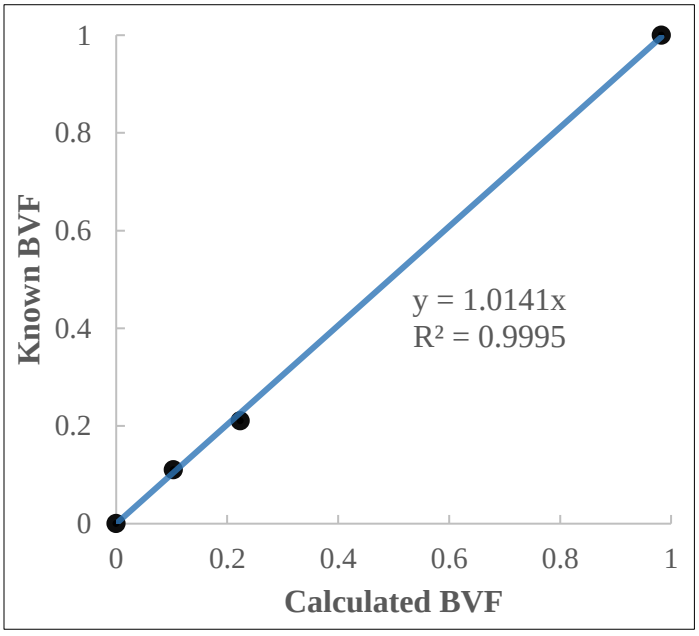

Figure A-2. Linear regression results for the known and calculated BVF's of the MRI phantom with a best fit line.

APPENDIX B: REGIONAL FAILURE LOAD ASSOCIATIONS

Further to the associations presented in Chapter 5, we explored the associations between the neck, intertrochanteric, and shaft failure loads. As the outcomes exhibited normal distributions, we used Pearson correlations to measure the strength of failure load association at the three critical regions. Statistical significance was set at $p < 0.01$. All statistical analysis was conducted using IBM SPSS Statistics 25.0 (Chicago, IL, USA). The von Mises stress failure load associations for the fall and stance loading configurations are reported in Table B-1.

Table B-1. Pearson correlation coefficients between the von Mises stress failure loads at the neck, intertrochanteric, and shaft regions. Significant associations are highlighted in the table ($p < 0.01$).

		Fall			**Stance**		
		Neck	*Intertrochanteric*	*Shaft*	*Neck*	*Intertrochanteric*	*Shaft*
Fall	*Neck*	1	0.816	0.578	0.833	0.709	0.671
	Intertrochanteric	-	1	0.798	0.720	0.608	0.563
	Shaft	-	-	1	0.478	0.312	0.398
Stance	*Neck*	-	-	-	1	0.780	0.807
	Intertrochanteric	-	-	-	-	1	0.732
	Shaft	-	-	-	-	-	1

We found that the failure loads between the stance and fall configuration were strongly associated with a mean correlation coefficient of 0.588 (range: 0.398 to 0.833). For the stance configuration, we observed strong associations between the neck, intertrochanteric, and shaft regions, with a mean correlation coefficient of 0.773 (range: 0.732 to 0.807). For the fall configuration, we observed strong associations between the neck, intertrochanteric, and shaft regions, with a mean correlation coefficient of 0.731 (range: 0.578 to 0.816).

APPENDIX C: LEAN MUSCLE AND INTRAMAT ASSOCIATION

We explored the associations between learn muscle and IntraMAT area measures at the upper thigh (~2 cm below the lesser trochanter). To evaluate, we used our MR participant data from Chapter 5 [150]. The lean muscle and IntraMAT areas of the 44 participants were calculated using subject specific thresholds as described in Chapter 5. We used Pearson correlations to measure the strength of association between the muscle and IntraMAT areas at the upper thigh.

For the fall and stance configuration, significant Pearson correlation coefficients ranged from 0.464 to 0.500 (Table C-1). In terms of specific functional groups, only the hip adductors and knee extensors offered significant associations between their muscle and IntraMAT areas.

Table C-1 . Pearson correlation coefficients between the lean muscle and IntraMAT areas at the upper thigh. Significant associations are noted in the table ($p < 0.01$).

	Muscle				
	Hip Extensor	*Hip Adductor*	*Hip Flexor*	*Knee Extensor*	*Total*
IntraMAT	0.027	0.464	0.082	0.500	0.280

The strongest, and significant, association between muscle and IntraMAT areas were found for the knee extensor and hip adductor group, or the two largest muscle area groups at the upper thigh. For these two groups, larger muscle area is associated with greater adiposity. These results suggest that for a relatively young adult population (mean age: 30.0, SD: 2.1 years), high IntraMAT area is not association to reduced muscle area. This result may be due to the relatively young adult population, whereby a decrease in muscle mass and progressive substitution by fat has not occurred as in elderly adults (65 years of age and older) [153]. Our findings are supported by previous research, where Holloszy et al. found that muscle area begins to decrease approximately 3-8% per decade after the age of 30 [154]. As our mean participant age of 30.0

years (SD: 2.1) is only approaching the threshold by Holloszy et al., the presence of IntraMAT is not correlated to low muscle.